Temperature Dependence of the Hypervelocity Impact Response of Polyethylene Plates from T_g to T_m

Jacob A. Rogers[1,2,3*], Aniket Mote[1], Sidney Davis[1], Paul T. Mead[4],
Charles U. Pittman, Jr.[5], Edwin L. Thomas[2],
Justin W. Wilkerson[1,2], Thomas E. Lacy, Jr.[1**]

[1]Department of Mechanical Engineering, Texas A&M University, College Station, TX 77843.
[2]Department of Material Science and Engineering, Texas A&M University, College Station, TX 77843.
[3] High Explosives Science and Technology, Q-5, Los Alamos National Laboratory, Los Alamos, NM 87545.
[4]U.S. Army Engineer Research and Development Center, Vicksburg, MS 39180.
[5]Department of Chemistry, Mississippi State University, Starkville, MS 39762.
[*]Corresponding author. Email: jacob_rogers@lanl.gov
[**]Corresponding author. Email: telacyjr@tamu.edu

Abstract

All spacecraft continue to face a growing risk of hypervelocity impacts (HVIs) by micrometeoroids and orbital debris (MMOD). Similarly, emerging hypersonic weapons pose acute ballistic threats to military and civilian assets. In both cases, the diminishing effectiveness of legacy armor demands the development of specialized, layered HVI protective structures. Ultra-high molecular weight polyethylene (UHMWPE) and high-density polyethylene (HDPE) stand out as promising intermediate layers due to their high specific energy absorption and tailorability. Yet, polyethylene's (PE's) behavior at HVI-induced strain rates ($>10^6$ s^{-1}) remains understudied and poorly understood, particularly near its glass transition (-116°C) and melt (130°C) temperatures. A recent HVI study revealed that UHMWPE targets impacted at room temperature exhibited bulk fragmentation while similar HDPE samples showed extensive melting and visco-plastic flow, as a consequence of differences in the two polymers' molecular mobility. In this current study, the interplay of target temperature (T_0), impact velocity (v_0), and average entanglements per chain (N_e) on PE's HVI response is investigated. 12.7 mm thick UHMWPE and HDPE plates at $T_0 = -120$°C, 23°C, and 140°C were subjected to 2.5 km/s and 6.0 km/s HVIs by 6.35 mm diameter aluminum spheres. The PEs' HVI responses were found to be largely governed by a competition between rates of strain and polymer chain relaxation. Lowering T_0 for a fixed N_e constrained chain motion analogous to increasing N_e at a fixed T_0. This caused HDPE's HVI response to increasingly align with UHMWPE's at similar v_0. The opposite was also observed. Increasing v_0 alone made both materials more prone to widespread fracture by raising strain rates beyond rates of chain disentanglement and reorientation. The material exhibiting the most visco-plastic flow without subsequent

bulk fragmentation lost less mass, had smaller perforations, and better absorbed energy. This suggested that for fixed T_0 and v_0, there is an optimal N_e value that maximizes a given PE's energy absorption. Increasing v_0 or decreasing T_0 requires a lower degree of entanglement to sustain the degree of molecular mobility that gives maximum energy absorption. These findings motivate the development of a protective structure composed of PE layers, each optimized for an anticipated average strain rate.

1 Introduction and Motivation

All manned and unmanned spacecraft face a significant threat of hypervelocity impacts (HVIs) from micrometeoroids and orbital debris (MMOD), with the danger from micrometeoroids escalating during long interplanetary voyages (*1, 2*). Similarly, emerging commercial and military hypersonic vehicles continue to present formidable challenges to legacy thermal and ballistic protection measures (*3–5*). HVI velocities exceeding 3 km/s (~Mach 9) can severely deform, erode, fracture, fragment, heat, melt, vaporize, and even sublimate materials, often leading to catastrophic system and mission failure, and/or loss of life (*6–8*). Numerically modeling the HVI response of materials generally involves a combination of constitutive and failure models and equations of state that are empirical in nature (*9*). For this reason, protective structure development and optimization usually involves costly HVI experiments *at room temperature* using sophisticated launch apparatuses, such as two-stage light gas gun (2SLGG) aeroballistic ranges (*10*). In many practical applications, materials not only see ultra-high impact velocities but also extreme environmental temperatures. Spacecraft in orbit, for example, can experience temperatures ranging −160°C to 120°C (*11*), while ambient temperatures on Earth can generally vary from −80°C to 50°C. Materials on the leading edges of hypersonic vehicles are subjected to temperatures exceeding ~2,000°C (*12*). Hence, characterizing the HVI response of materials at extreme operating temperatures through methodical laboratory tests is essential for the development and application of next-generation protective structures.

Many spacecraft utilize polymers as window materials or as intermediate layers in MMOD (Whipple) shields (*13, 14*), while ballistic "bulletproof" vests often incorporate polymer composites for enhanced energy absorption (*15*). The effectiveness of polymers and polymer composites in these applications, combined with their customizable properties, make them attractive candidate

materials for innovative space and military protective structures. Numerous investigations have been performed on the room temperature HVI response of polycarbonate (PC), polymethyl methacrylate (PMMA), and polyethylene (PE) and their composites (*16–21*). In these studies, targets were typically subjected to normal HVIs by projectiles representing anticipated threats (spacecraft debris, dust, ice, *etc.*). High-rate diagnostics and post-impact target characterization methods were used to characterize HVI-induced target deformation and failure, as well as identify predominant energy absorbing mechanisms. Ultra-high molecular weight PE (UHMWPE) and high-density PE (HDPE) were particularly promising intermediate layers in protective structures due to their high tailorability, low density and cost, and relatively high energy dissipation capabilities (*22, 23*). Despite their potential use in extreme environments, these PEs have not been systematically studied under extreme strain rate and temperature conditions. In fact, there have been very few HVI experiments at cryogenic temperatures involving *any* type of material (*24–26*), and even fewer investigations involving targets pre-heated well above room temperature (*27*).

UHMWPE and HDPE are commercially available semi-crystalline polymers of $(–C_2H_4–)_n$ that share similar densities (ρ_0 = 0.95 g/cc) and physical appearances. They primarily differ in average molecular chain length (*i.e.*, degree of polymerization, n) or, equivalently, average molecular weight (*28, 29*). The average molecular weight is much higher for UHMWPE ($M_w > 3,000$ kg/mol) than for HDPE (M_w = 100–500 kg/mol) (*30*). The longer chains in UHMWPE lead to fewer chain ends per unit weight and more entanglements per chain (N_e = 3,000–8,000) compared to HDPE (N_e = 120–250). UHMWPE can be over 60 times (6,000%) more entangled than HDPE! Entanglements generally boost material toughness and deformation resistance by creating an energy-absorbing network of interlocked polymer chains that inhibits chain mobility, uniformly distributes stresses, increases elasticity, and reduces crack propagation (*31–35*). UHMWPE's entanglements lead to a melt viscosity of around 10^{10} Pa·s, roughly 10^7 times more than HDPE's ($<10^3$ Pa·s), which hinders standard high shear processing (*36*). The differences in N_e and molecular weight influence molecular packing,[1] resulting in different degrees of crystallinity (40–75% in UHMWPE and 70–80% in HDPE) and crystalline structure sizes (*29, 34*). Chain branching also affects PE's mechanical behavior. Less branching generally promotes increased crystallinity and density, making processing challenging (*37, 38*). Thus, commercial PEs often have been designed to have some degree of short

[1] N_e inhibits the growth of parallel chain folding crystals.

chain branches to facilitate manufacturing (*e.g.*, CH_3 groups adjust molecular conformation to reduce melt viscosity). Although detailed information on chain branching and comonomer content is limited, most commercial PEs are remarkably linear (<3% branching) and pure (additives levels <5% by weight) to avoid impeding powder fusion during molding and to preserve mechanical properties (*30*). UHMWPE typically has greater tensile strength, abrasion and crack resistance, and *ballistic* impact strength due to these morphological variations. UHMWPE is used in high-wear applications such as medical devices (*e.g.*, knee joint replacements) and bulletproof vests in the form of Spectra® or Dyneema® gel spun fibers (*39*). HDPE, with its higher crystallinity, offers a higher tensile modulus but lower strength and wear resistance (*40*). HDPE is commonly found in containers and corrosion-resistant piping. Both exhibit excellent chemical resistance. However, their mechanical and dynamic mechanical property differences at extreme temperatures *and* very high strain rates have not been well characterized.

Like many polymers, PE's mechanical properties and dynamic behavior are highly sensitive to strain, strain rate, temperature, and pressure. At room temperature, UHMWPE shows significant strain hardening in tension and compression at strain rates up to $\dot{\varepsilon} = 10^3$ s^{-1} for strains under 300% (*40,41*). HDPE, however, demonstrates nearly perfectly plastic behavior across similar strains and strain rates (*40, 42*). HDPE undergoes significant adiabatic heating and thermal softening at rates above $\dot{\varepsilon} = 10^{-2}$ s^{-1} (*43*). The effective thermal plastic work conversion factor ($0 < \beta < 1$) quantifies the portion of plastic work converted into heat. HDPE tends to covert nearly all plastic work to heat ($\beta \approx 1$), while UHMWPE converts less than half ($\beta < 0.5$) (*29, 43*). The *ballistic* impact resistance and deformation behavior of these PEs are well-documented for impact velocities $\sim 10^2$ m/s and $\dot{\varepsilon} < 10^5$ s^{-1} (*29, 35, 44–46*). Generally, higher molecular weight enhances impact strength, increases resistance to thermal softening/melting, and inhibits crack propagation (*47, 48*). Increased crystallinity does improve yield strength but at the cost of impact performance (*29,49,50*). At and above room temperature, UHMWPE has slightly better ballistic performance than HDPE (*29, 51*). However, characterizing the effects of polymer structure and morphology on PE behavior at HVI-induced strain rates ($\dot{\varepsilon} = 10^6$–10^8 s^{-1}) remains a challenge. For PEs, the time-temperature superposition principle (*43*) may be used to relate low-rate material data to that for higher rates. In essence, a one decade increase in $\dot{\varepsilon}$ corresponds to a 10°C drop in polymer temperature. When the time temperature superposition was applied to results from quasi-static test at markedly reduced

temperatures corresponding to HVI-induced strain rates for both PEs, HDPE still showed significant thermal softening (*43*). In contrast, at these same temperatures UHMWPE demonstrated only mild softening and continued to exhibit strain hardening (*43*). This implies that the differences in thermal softening (adiabatic heating) between the two materials stems from microstructural factors. These findings are consistent with molecular dynamics (MD) simulations of various PEs subjected to strain rates over 10^6 s^{-1}, which predicted a combination of strain hardening, thermal softening, and a linear relationship between yield stress and logarithmic strain rate (*52–54*).

Some efforts have been made to characterize PE's HVI behavior. For example, Cha *et al.* (*23*) conducted HVI tests at approximately 4 km/s using 5.56 mm diameter aluminum projectiles. UHMWPE targets showed superior HVI performance compared to Kevlar used in stuffed Whipple shields (*i.e.*, lightweight, energy-absorbing layers sandwiched between a series of metallic plates). Bowering (*55*) conducted HVI experiments with 4 mm diameter aluminum spheres impacting UHMWPE, HDPE, and PMMA plates at 2.0–6.5 km/s. UHMWPE appeared to absorb more impact energy. However, these studies were more qualitative in nature and raised further questions about PE's fundamental ultra-high strain rate behavior. Rogers *et al.* (*22*) compared 6.35 mm thick UHMWPE ($M_w = 4.7 \times 10^6$ g/mol) and HDPE ($M_w = 1.7 \times 10^5$ g/mol) plates subjected to 2.0–6.5 km/s HVIs by 10 mm diameter aluminum spheres. For impact velocities near 2.0 km/s, the impactor was significantly deformed and eroded but largely remained intact. As the velocity was increased, the projectiles progressively fractured and became more pulverized. Regardless of impact velocity, UHMWPE showed a more quasi-brittle response (*i.e.*, extensive fragmentation in the ejecta and debris cloud), likely driven by its highly entangled (constrained) chains. In contrast, HDPE exhibited substantial bulk-melting and large-scale visco-plastic deformation due to intense adiabatic heating (Fig. 1). Despite having similar debris cloud geometries and leading-edge velocities, UHMWPE targets lost about 40% more mass than HDPE targets for a given impact velocity, indicating potentially greater total momentum and kinetic energy in the UHMWPE debris clouds. HDPE targets had perforation radii around 20% larger than those in UHMWPE. Initial SEM analysis also revealed that UHMWPE fracture surfaces were flat and resembled brittle fractures; HDPE surfaces exhibited drawn oriented fibrils, thermal melting/softening, and flow.

The bulk behavior of PE at ultra-high strain rates is highly temperature-dependent. For semi-crystalline polymers, higher temperatures generally lead to increased free volume and chain mo-

bility, faster disentanglement rates, shorter relaxation times, reduced viscosity in noncrystalline regions, and ultimately earlier and more complete melting (*34*). Conversely, lowering the temperature has the opposite effect. Such temperature-related phenomena are often characterized in terms of the polymer's glass transition temperature (T_g) and melt temperature (T_m). For both UHMWPE and HDPE, $T_g = -116°\text{C}$ and $T_m = 130°\text{C}$. Below T_g, the free volume is minimal, and PE chain segment motion is highly constrained. Above T_g, a significant increase in free volume enhances chain mobility, resulting in a transition from a glassy to a rubbery state. However, this transition primarily affects the noncrystalline regions; crystalline regions remain largely intact, interconnected by tie molecules and inter-crystalline links that span the amorphous regions. Chain entanglements also contribute to stiffness above T_g. Near and above T_m, thermal energy overcomes intermolecular forces holding the crystals together, causing them to melt. UHMWPE and HDPE then become viscous liquids, with UHMWPE showing particularly high viscosity due to its dense entanglements. At temperatures much higher than T_m, the PEs start to decompose *via* pyrolysis and combustion. This temperature dependent behavior in PE is well characterized for relatively low loading rates ($\dot{\varepsilon} \lesssim 10^2\ \text{s}^{-1}$) (*43, 56–58*). However, there have been no comprehensive studies on semi-crystalline

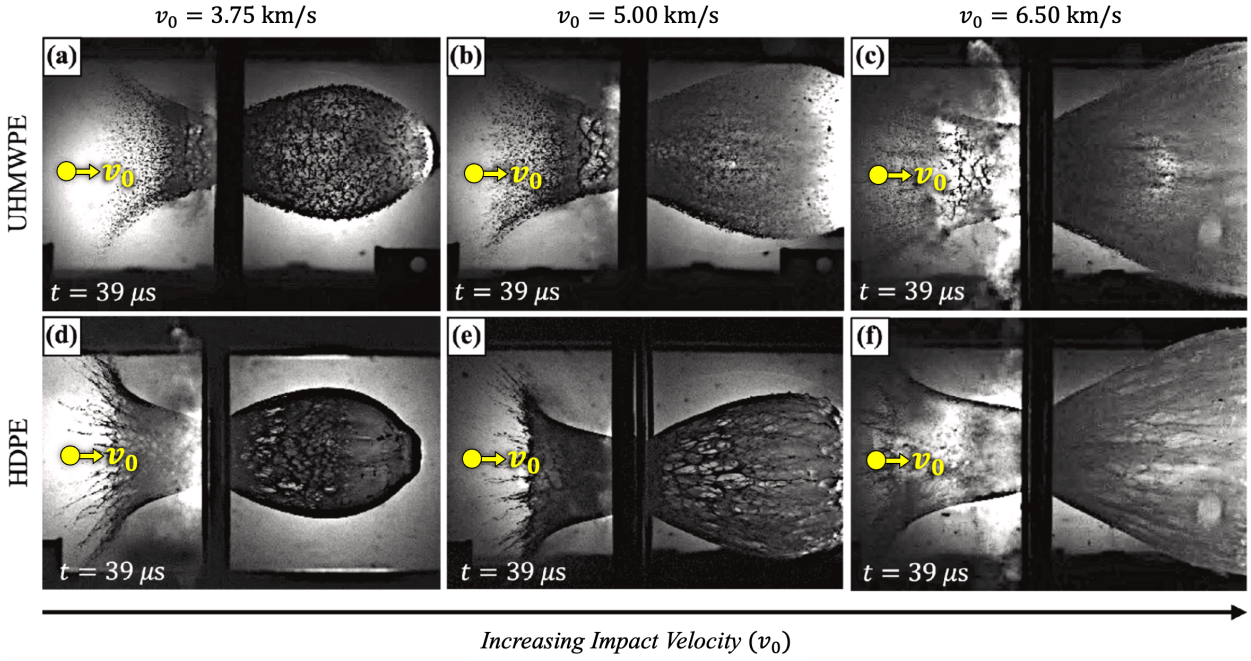

Figure 1: Comparing fully-developed ejecta and debris clouds at different nominal impact velocities in the tested range: (a–c) UHMWPE and (d–f) HDPE. With increasing nominal impact velocity (from left to right), UHMWPE debris fragments become smaller on average, and bulk melting in HDPE becomes more pronounced. Reprinted from Ref. (*22*).

PE's HVI ($\dot{\varepsilon} \gtrsim 10^6$ s^{-1}) response at temperatures that span the glass transition (T_g) and melt (T_m) temperatures. Addressing this gap is key to understanding the mechanisms governing PE's dynamic behavior and its performance in extreme environments.

Despite their similar density, crystallinity, and chemistry, UHMWPE and HDPE have distinct phenomenological responses to HVI, due to their significant differences in average number of entanglements per chain (N_e). HVI induced adiabatic shock heating and rapid plastic deformation quickly induce strong gradients in the local temperature, strain, strain rate, and stress fields that evolve spatially and temporally. PE's poor thermal conductivity intensifies the localized heating. In the HVI tests conducted by Rogers *et al.* (*22*), HDPE plates exhibited perforation volumes ~1.4 times larger than those for identical tests performed on UHMWPE plates. The average size (pervaded volume) of the UHMWPE chains was roughly 150 times larger than that of the HDPE chains, as estimated by their unperturbed RMS end-to-end distances and molecular weights (*59*). These estimates suggest that perhaps 200 times more HDPE chains were involved in deformation, heating, *etc.* compared to UHMWPE chains. For the molecules undergoing rapid deformation, the temperature increase quickly enhances free volume and chain mobility, facilitating chain disentanglement and shortening relaxation times. HVI-induced temperatures can readily exceed the melt temperatures (T_m) of UHMWPE and HDPE, encouraging bulk melting and flow. However, PE's average molecular weight (chain length) is proportional to the average number of entanglements per chain (N_e) and inversely proportional to the nominal disentanglement rate. When this disentanglement rate is surpassed by the local HVI-induced loading rate, the entangled molecular network likely becomes virtually frozen, causing internal stresses to rise until chain scission occurs. The motivating hypothesis of this study is that this phenomenon manifests macroscopically as brittle failure and bulk fragmentation.

To test this hypothesis, we investigate how the interplay between pre-impact target temperature (T_0) and impact velocity (v_0) governs the ultra-high strain rate response of PE, with emphasis on the transition between melting- and fragmentation-dominated regimes. 12.7 mm thick UHMWPE and HDPE plates, conditioned to temperatures spanning $T_0 < T_g = -116$°C to $T_0 > T_m = 130$°C, were subjected to HVIs by 6.35 mm-diameter 2017-T4 aluminum spheres at velocities of 2.5 and 6.0 km/s. The responses of the two PEs were quantified using a combination of pre-impact materials characterization, *in-situ* high-speed imaging, and post-impact forensic analyses. The PE

materials were identical to those used in our previous work (*22*), in which room-temperature impacts revealed distinct behaviors: UHMWPE exhibited large-scale quasi-brittle fragmentation, whereas HDPE exhibited bulk melting. In this current study, we demonstrate that the HVI response of HDPE transitions from bulk melting to quasi-brittle fragmentation as the T_0 is reduced below the PE glass transition temperature (*i.e.*, similar to the room temperature response of UHMWPE). Similarly, as the T_0 was increased beyond the melting temperature ($T_0 > T_m$), UHMWPE displayed bulk melting consistent with the room temperature behavior of HDPE. The variations in HVI-induced deformation and failure were significantly dependent on T_0, strongly suggesting that microstructural characteristics, particularly the degree of chain mobility, are responsible for the distinct HVI behaviors of UHMWPE and HDPE observed at room temperature. Numerical simulations of HVIs to PE were used to infer impact-induced target temperatures, strains, and strain rates.

2 Methods

This section provides an overview of the UHMWPE and HDPE materials and HVI experimental methodology (target sample preparation, fixturing, passive target cooling and heating techniques, *etc.*) used in this study. An overview of the numerical simulation approach is briefly detailed.

2.1 Materials and Sample Preparation

Similar to the work performed in Ref. (*22*), monolithic plates of UHMWPE and HDPE with dimensions 600 x 600 x 12.7 mm^3 were sourced from Mitsubishi Chemical Advanced Materials (TIVAR® 1000) (*60*) and King Plastic Corporation (King KPC® HDPE) (*61*), respectively. TIVAR® 1000 (compression molded GUR 4120 powder) has over 97% purity ($\lesssim$3% processing/lubrication additives) and an average molecular weight of $M_w = 4.7 \times 10^6$ g/mol, as calculated from its melt viscosity using the Margolies equation (*62, 63*). The King KPC® HDPE plates were also prepared *via* compression molding, without the use of any additives (*64*). The as-received PE plates were cut into smaller 102 x 102 x 12.7 mm^3 HVI targets using a band saw. For the remainder of this paper, "UHMWPE" denotes TIVAR® 1000 and "HDPE" refers to King KPC® HDPE. Zhang *et al.* (*64*) characterized the molecular weight distribution of this HDPE using gel permeation chromatography, reporting number average, weight average, and Z-average molecular weights of

Table 1: Material characterization data for UHMWPE (TIVAR® 1000) and HDPE (King KPC® HDPE). Molecular weights for UHMWPE and HDPE were sourced from Refs. (*62, 63*) and (*64*), respectively. Additional data, including TGA, DSC, and DMA results previously reported in Ref. (*22*) are also included. Key mechanical properties were sourced from Refs. (*60, 61*).

Property	UHMWPE	HDPE	% Difference	Standard(s)
Number average molecular weight, M_n [g/mol]	···	1.8×10^4	···	···
Weight average molecular weight, M_w [g/mol]	$4.7 \times 10^{6\dagger}$	1.7×10^5	190%	···
Z-average molecular weight, M_z [g/mol]	···	1.0×10^6	···	···
Polydispersity index, $PDI = M_w/M_n$	···	9.6	···	···
Entanglement molecular weight, M_e [g/mol]	1,250‡	1,250‡	0%	···
Average entanglements per chain, $N_e = M_w/M_e$	3,800	140	190%	···
Glass transition temperature, T_g [°C]	−116.1	−116.2	0.1%	ASTM E1640-18
Melting temperature, T_m [°C]	134.1	131.1	2.3%	ASTM F2625, D3418
Crystallinity, χ [%]	52.5	70.2	28%	ASTM F2625, D3418
Initial decomposition temperature, IDT [°C]	439.1	423.2	3.7%	ASTM E2550
Density, ρ [g/cc]	0.927	0.954	2.9%	ASTM D792
Yield strength, σ_y [MPa]	40	31	25%	ASTM D638
Elastic modulus, E [GPa]	0.55	1.8	110%	ASTM D638
Thermal conductivity, [W/(K·m)]	0.4	0.5	22%	···
Izod Impact Resistance	no break	1.1	···	ASTM D256
Shore D Hardness	66	68	3%	ASTM D2240
Specific heat capacity, c_v [kJ/(kg·K)]	1.8	2.3	24%	···

†This M_w value was determined using the Margolies equation (*63*). Hence, M_n, M_z, and PDI values are not reported for UHMWPE. ‡This M_e value is generally accepted for linear PE in the melt state (*66, 67*)

$M_n = 1.8 \times 10^4$ g/mol, $M_w = 1.7 \times 10^5$ g/mol, and $M_z = 1.0 \times 10^6$ g/mol, respectively. The polydispersity index (PDI) was $PDI = M_w/M_n = 9.6$. Acquiring comparable chromatographs for UHMWPE is generally challenging due to its high viscosity and limited solubility (*30, 65*). Consequently, TIVAR® 1000 UHMWPE's PDI was not available, but was presumed to be $PDI \approx 10$, consistent with other commercial UHMWPEs (*65*). Rogers *et al.* (*22*) reported measured T_g, T_m, density (ρ_0), crystallinity (χ), and initial decomposition temperature (IDT) values for each PE, which aligned well with supplier and literature values (Table 1). $T_g = -116$°C for both PEs, while $T_m = 134$°C and 131°C for UHMWPE and HDPE, respectively. The UHMWPE density and crystallinity ($\rho_0 = 0.93$ g/cm^3 and $\chi = 52\%$) were lower that those for HDPE ($\rho_0 = 0.95$ g/cm^3 and $\chi = 70\%$). UHMWPE experienced an onset of thermal decomposition at a slightly higher temperature (439°C) compared to HDPE (423°C).

The semi-crystalline structure of UHMWPE and HDPE complicates precise determination of their entanglement density per volume (ν_e) and per chain (N_e) values. A simple approach to estimate N_e in the melt state involves dividing the weight average molecular weight (M_w) by the

entanglement molecular weight (M_e, *i.e.*, $N_e \sim M_w/M_e$), where $M_e = 1,250$ g/mol is an accepted nominal M_e value for linear PE in the melt state (*66, 67*). Using this M_e value, $N_e = 3,800$ and $N_e = 140$ monomer for UHMWPE and HDPE, respectively. Hence, UHMWPE's chains are about 30 times more entangled than HDPE's (*cf.* Table 1).[2] These calculations, while not accounting for the full effect of molecular weight distribution or crystalline regions, do highlight that the primary distinction between the PEs lies in their N_e values (and molecular weight).

2.2 The Impact Experiments

Normal HVI experiments were conducted on UHMWPE and HDPE plates (nominal thickness, $h_t = 12.7$ mm) using a 12.7 mm bore 2SLGG to launch 2017-T4 aluminum spheres ($d_p = 6.35$ mm) at two distinct impact velocities ($v_0 = 2.6$, 6.0 km/s). The ratio of target thickness to projectile diameter ratio ($h_t/d_p = 2$) was held fixed in all tests. Hence, six HVI experiments per PE type (12 total) were conducted. Each projectile was launched into an enclosed aeroballistic range with backfill pressure $P = 13$ kPa of nitrogen. Further details on the 2SLGG aeroballistic range and testing methodology can be found in Refs. (*10, 22, 68*). As an aside, the ratio $h_t/d_p = 2$ was three times greater than for similar room temperature PE experiments performed by Rogers *et al.* (*22*), *i.e.*, h_t was increased to increase the thermal mass of the target to better maintain the nominal target temperature (T_0) during testing ($T_0 = -120°\text{C} < T_g$, $T_0 = 23°\text{C}$ (room temperature), and $T_0 = 140°\text{C} > T_m$). Figure 2 presents a schematic overview of these experiments.

2.3 Cooling and Heating the Polyethylene Plates

Prior to low- and elevated-temperature HVI testing, benchmark experiments were performed in laboratory air to assess the rate-of-change in target mid-plane temperature from some prescribed initial value. For example, all four PE targets impacted at a mid-plane temperature $T_0 = -120°\text{C}$ were first cooled to $T_0 = -180°\text{C}$ before being placed in the target tank. After sealing the tank, roughly 10 minutes was required to evacuate the tank and backfill with N_2 to the required vacuum pressure

[2] As crystals form, they drive entanglements to their surfaces, leaving few or no entangled chains within the crystal itself. This process elevates the number of entanglements per volume (entanglement density) in the noncrystalline regions by a factor of $1/(1-\chi)$. Consequently, HDPE concentrates entanglements into its noncrystalline regions by a factor of ~1.6 times greater compared to UHMWPE.

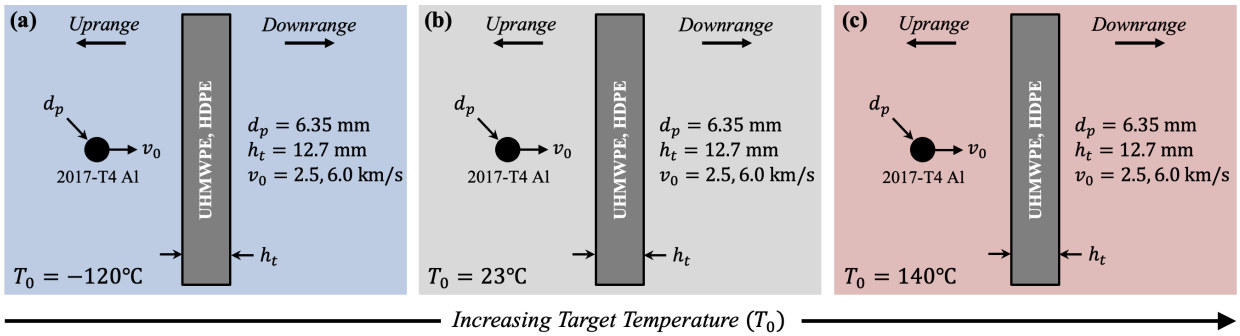

Figure 2: An overview of the HVI testing method. For UHMWPE and HDPE, 600 x 600 mm^2 square plates of thickness h_t = 12.7 mm were subjected to v_0 = 2.5 and 6.0 km/s impacts at T_0 = (a) −120°C, (b) 23°C, and (c) 140°C, resulting in 12 total HVI experiments.

(13 kPa). Hence, the time it takes for the specimen to warm to the desired impact temperature must exceed the required vacuum time ($t_{vac} \approx 10$ min). Initial benchmark experiments were conducted to characterize the time for the mid-plane temperature of a PE plate to warm from $T_0 = -180$°C to the glass transition temperature ($T_0 = T_g = -116$°C); the internal plate temperature was monitored using thermocouples. An individual HDPE plate was soaked in a liquid nitrogen (LN_2) bath for about two hours, then exposed to laboratory air at 23°C. It took roughly 8 min for the mid-plane temperature to reach T_g, which was *less* than the requisite vacuum time, t_{vac} (Fig. 3a). Moreover, the PE surface temperature will generally exceed the mid-plane temperature by about 5–7°C based upon simple two-dimensional (2D) heat transfer calculations (*cf.*, Section S1). As a consequence, a high thermal mass target fixture was developed to extend the time for a target to achieve the desired testing temperature beyond t_{vac}, similar to the approach implemented by Warren *et al.* (*69*). To illustrate, when a PE plate was sandwiched between two 12.7 mm thick steel plates and soaked in LN_2, the in-laboratory warming time exceeded the vacuum time by roughly four minutes (this difference would undoubtedly increase for a plate assembly under partial vacuum in the target tank). A specialized high thermal mass target fixture was developed to encase a PE plate within machined steel plates (minimum thickness, 12.7 mm); the uprange and downrange surfaces included 76 mm diameter circular apertures (windows) that aligned with the projectile impact axis (Figs. 3b and 3c). Optional window covers were developed to further insulate the targets but were unnecessary in this study. In lab air tests, the specialized fixture extended the target warming times to over 15 minutes, *i.e.*, 5 min beyond t_{vac}. Hence, for the HVI experiments performed at $T_0 < T_g$, the as-received PE plates cut to 102 x 102 x 12.7 mm^3 (Fig. 4a) were placed in the target fixture (Fig. 4b), submerged

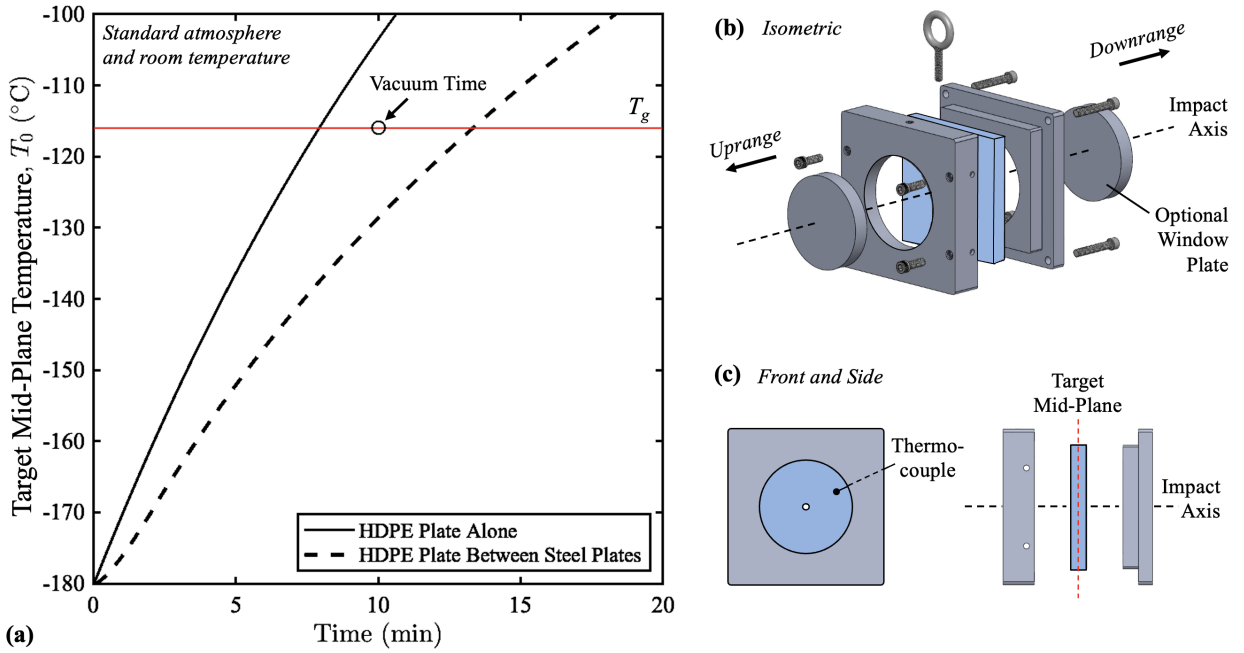

Figure 3: Fixture development for cold-temperature HVI experiments: (a) plot of the measured mid-plane temperatures of an HDPE plate alone and an HDPE plate sandwiched between two steel plates. Figure (b) displays an exploded view of the high thermal mass target fixture, with (c) showing the approximate thermocouple placement within the target mid-plane.

in a LN_2 bath for two hours (Fig. 4c), and rapidly transferred to the target tank (Fig. 4e). The tank was immediately sealed and the vacuum pump initiated. A thermocouple, positioned a radial distance about 30 mm from the projectile axis, recorded target plate mid-plane temperatures in the exposed window region (Fig. 3c). When the measured mid-plane temperature reached T_0 = 120°C, the 2SLGG was fired, accelerating the aluminum spheres to either 2.5 or 6.0 km/s. For all HVI experiments, the projectile perforated the target roughly twice as fast as the time required for shock waves to reflect off the boundaries and return to the impact site (see Section S2). Thus, the fixture boundaries had no influence on the perforation event. The clamped boundary conditions may have a minor influence on the targets' post-perforation responses. Nonetheless, since the targets were all tested identically, a direct comparison between their responses is reasonable.

The high-thermal mass target fixture (Fig. 3b) was also used in all elevated target temperature HVI experiments (nominal mid-plane temperature at impact, T_0 = 140°C). Prior to heating, each of the four 102 x 102 x 12.7 mm^3 PE targets were sandwiched between two 100 x 100 x 0.050 mm^3 square Mylar (polyethylene terephthalate) sheets to maintain target thickness and promote planarity after target melting (*i.e.*, prevent target bulging along impact axis). Mylar maintains its

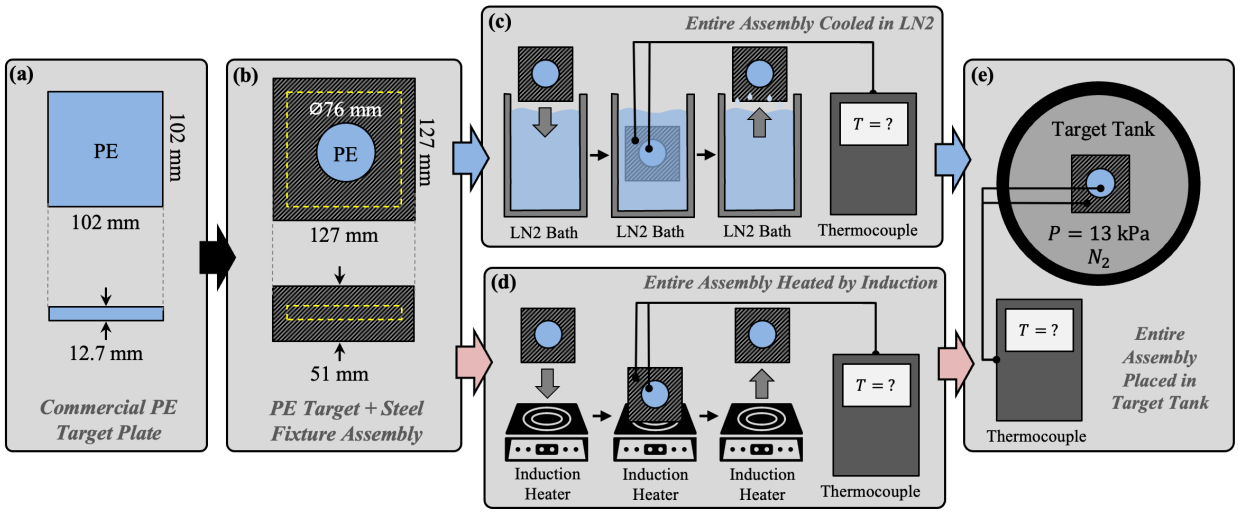

Figure 4: The cooling and heating methodology for the HVI experiments. The (a) as-received PE plates cut to 102 x 102 x 12.7 mm^3 were (b) placed in the target fixture, either (c) submerged in a LN_2 bath for two hours or (d) placed on an induction burner for 60 minutes, and (e) rapidly transferred to the target tank. Target through-thickness mid-plane and surface temperatures were monitored using thermocouples.

mechanical strength up to about 150°C and is suitable for use up to 200°C under moderate loads. The Mylar sheets constrained the pre-impact, molten PE targets without significantly affecting their HVI performance, since the projectile interacted with 130 times more PE than Mylar (by volume). The UHMWPE and HDPE targets were initially inductively heated from room temperature to T_0 = 170°C inside the fixture (Fig. 4d). The target and fixture temperatures were monitored using thermocouples and infrared thermometry, respectively. Roughly 30 minutes were required to equilibrate the temperature in the assembly. For $T_0 \geq 130$°C, both materials became transparent and more pliable, though they showed no significant signs of flow (the heated plates largely retained their original shape). After heating, each target assembly was quickly moved to the target tank, which was then sealed and evacuated to a partial pressure of 13 kPa (Fig. 4e). Similar to the cold temperature experiments, the mid-plane temperature of the PE targets was continuously monitored using thermocouples. The projectile was launched once the nominal target mid-plane temperature reached T_0 = 140°C . After impact and removal from the target tank, the target and fixture assembly was quenched in LN_2 to preserve residual impact-induced deformation and damage

In addition, four room temperature HVI experiments (T_0 = 23°C) were also performed. Since no extra thermal mass was needed, the targets were sandwiched between two 4.8 mm thick steel plates each with a 100 mm diameter circular aperture, similar to the method used in Ref. (*22*).

The room temperature PE target assembly was then placed in the target tank, and once the backfill pressure reached 13 kPa, the projectile was launched.

In each experiment, a Shimadzu HPV-X2 high-speed camera, operating at 1 MHz, captured the HVI event *in-situ*, including the projectile's approach, impact, and perforation, as well as the ensuing expansion of the projectile/target ejecta and debris clouds (128 total images per experiment). The camera was oriented orthogonal to the impact axis and configured for shadowgraphic imaging, yielding high-contrast, stop-motion images, consistent with previous HVI experiments (*cf.* Fig. 1) (*22*). These images were vital in evaluating how T_0 affected target failure and bulk response, and were used in conjunction with motion tracking software to measure the horizontal velocity of the debris cloud's leading edge (*i.e.*, "debris cloud tip velocity") (*22*). The PE plates were weighed pre- and post-HVI to determine target mass loss (Δm_t). For a number of impacted targets, the perforations were mostly circular in the plane but had irregular/jagged edges. The opening diameter somewhat increased from the front to the back of the target in the through-thickness direction, resulting in a conical perforation surface. For these reasons, the ImageJ software was used to trace the inner-most perimeter of each perforation to measure an effective perforation area (A_e). This area was then used to calculate an effective perforation diameter ($d_e = \sqrt{4A_e/\pi}$), representing the diameter of a circle with equivalent area.

2.4 Numerical Simulations of HVIs to PE

The Elastic Plastic Impact Computation (EPIC) code (*70*) was used to predict the HVI-induced equivalent plastic strain, strain rate, and temperature distributions in HDPE targets as a function of nominal target temperature (T_0) and impact velocity (v_0). EPIC is a hybrid code that couples traditional finite elements with smooth particle hydrodynamics (SPH) to model large-scale deformation, fracture, and fragmentation. Idealized three-dimensional (3D) quarter-symmetry models of projectiles and targets were developed using tetrahedral finite elements (total number of elements, $\sim 3 \cdot 10^6$), where the characteristic element size increased with radial distance from the impact axis. The projectile and target mesh sizes matched in the contact region, and a mesh sensitivity analysis confirmed solution convergence. A finite-element-to-particle conversion was implemented whenever the equivalent plastic strain reached 30%, a standard value for ductile materials (*71*).

Projectile and HDPE target material behaviors were captured using a Mie-Gruneisen equation of state (*72*), Jonson Cook (JC) constitutive model (*73*), and JC fracture model (*74*), with parameters sourced from Ref. (*75*) and the EPIC materials library. Material parameters for UHMWPE were unavailable. Consequently, six simulations of HVIs to HDPE targets were used to infer the *continuum* response of both polymers during the early stages of target perforation. Fundamental differences in the behavior of UHMWPE and HDPE are also likely driven by differences in crystallinity, degree of chain entanglement, and other microstructural and chemical features that cannot be captured by a continuum-based code like EPIC.

3 Hypervelocity Impact Experimental Results and Discussion

This section details key experimental results for the 2.5 km/s and 6.0 km/s HVIs on the 12.7 mm thick UHMWPE and HDPE plates, whose measured nominal pre-impact temperatures were at $T_0 = -120$°C, 23°C, and 140°C. *In-situ* high-speed images of the HVIs, optical images of target perforations, and performance metric plots were generated across the full test matrix. Table 2 summarizes the impact velocity (v_0), target temperature (T_0), normalized target mass loss ($\Delta m_t/m_p$), normalized effective perforation diameter (d_e/d_p), and normalized debris cloud tip velocity (v_{dc}/v_0) for the twelve temperature-controlled HVI experiments. Rows are grouped by target temperature; within each temperature group, UHMWPE and HDPE tests are paired at comparable low and high impact velocities, with alternating shading highlighting the velocity pairs. Impact velocities varied across the experiments, with measurements at $v_0 = 2.49 \pm 0.25$ km/s and $v_0 = 6.17 \pm 0.10$ km/s for each desired nominal v_0 value. Subtle variations in v_0 values had little effect on impact loading conditions (*i.e.*, temperature, stress, strain, and strain rate distributions) compared to that resulting from the ~150% increase from $v_0 \approx 2.5$ km/s to $v_0 \approx 6.0$ km/s (*cf.* Fig. S5). T_0 measurements varied within a range of ±2°C and corresponded to PE plate mid-plane temperatures in the aperture/window region of the fixture (*cf.* Fig. 3c).

Table 2 highlights several important trends in normalized mass loss, including clear reversals in the relative response of UHMWPE and HDPE with temperature. Recall that room temperature HVIs to PE targets performed by Rogers *et al.* (*22*) demonstrated that HDPE targets had roughly 40% less mass loss than UHMWPE targets for a given impact velocity. In contrast, for the cold

temperature tests ($T_0 = -120$°C) performed at $v_0 \approx 2.5$ km/s in this study, HDPE exhibits a substantially *greater* normalized mass loss ($\Delta m_t/m_p = 6.42$) than UHMWPE ($\Delta m_t/m_p = 1.10$). A similar pattern is observed for cold targets impacted at $v_0 \approx 6.0$ km/s, where HDPE exceeds UHMWPE in normalized mass loss (86.83 *vs.* 68.01). For room temperature tests ($T_0 = 23$°C) performed at $v_0 \approx 2.5$ km/s, HDPE exhibits a substantially *lower* normalized mass loss ($\Delta m_t/m_p = 0.73$) than UHMWPE ($\Delta m_t/m_p = 2.39$) consistent with the results reported in Ref. (*22*). Similar results were observed for room temperature targets as the impact velocity was increased to 6.0 km/s, where $\Delta m_t/m_p = 7.98$ and 13.60 for HDPE and UHMWPE, respectively. For tests performed above the PE melting temperature (*i.e.*, $T_0 = 140$°C), HDPE targets exhibited less mass loss than UHMWPE at both velocities. These results demonstrate a clear crossover in material response with temperature. The normalized debris cloud tip velocity (v_{dc}/v_0) provides additional insight into relative energy absorption. For all conditions, UHMWPE exhibits values that are comparable to or greater than those of HDPE. Notably, HDPE at $T_0 = 140$°C shows the lowest v_{dc}/v_0 values across all tests, suggesting enhanced energy absorption under these conditions. This behavior reflects a temperature-dependent competition between polymer chain mobility and entanglement constraints. At low T_0, reduced free volume and long relaxation times effectively immobilize chains, promoting brittle fragmentation—particularly in HDPE, which lacks the dense entanglement network of UHMWPE—leading

Table 2: A summary of the temperature-controlled HVI experiments performed in this study (twelve total), including measurements of impact velocity, mass loss, and effective perforation diameter.

No.	Material	v_0 (km/s)	T_0 (°C)	$\Delta m_t/m_p$	d_e/d_p	v_{dc}/v_0
1	UHMWPE	2.64	-120	1.10	1.33	0.40
2	HDPE	2.40	-120	6.42	1.60	0.40
3	UHMWPE	6.10	-120	68.01	7.77	0.42
4	HDPE	6.20	-120	86.83	7.83	0.41
5	UHMWPE	2.20	23	2.39	1.14	0.47
6	HDPE	2.20	23	0.73	1.42	0.44
7	UHMWPE	6.30	23	13.60	3.25	0.46
8	HDPE	6.20	23	7.98	4.65	0.45
9	UHMWPE	2.69	140	33.60	4.17	0.48
10	HDPE	2.78	140	9.86	1.50	0.37
11	UHMWPE	6.00	140	90.32	8.87	0.46
12	HDPE	6.20	140	36.10	6.33	0.35

v_0, actual projectile impact velocity; $m_p = 0.372$ g, projectile mass; $d_p = 6.35$ mm, projectile diameter; T_0, target temperature; $\Delta m_t/m_p$, normalized mass loss; d_e/d_p, normalized effective perforation diameter; v_{dc}/v_0, normalized debris cloud velocity.

to increased mass loss. At intermediate T_0, HDPE can accommodate deformation through visco-plastic flow while UHMWPE remains more constrained and fragmentation-prone, reversing their relative responses. At elevated T_0, increased free volume and reduced relaxation times enable HDPE chains to more readily disentangle and undergo sustained visco-plastic flow, prolonging energy dissipation, whereas UHMWPE's highly entangled network remains prone to stress accumulation and subsequent melt fracture under rapid loading. These deformation and failure mechanisms are examined in greater detail throughout the remainder of this section.

In HVI shielding applications, the debris cloud generally poses a more significant threat to downrange assets, personnel, or infrastructure than the corresponding ejecta cloud. In addition, the debris cloud contains most of the failed projectile/target material. For these reasons, the following discussion prioritizes debris cloud formation, expansion, and characteristics, although the ejecta cloud displays similar features. For each of the twelve HVI experiments, the high-speed camera captured shadowgraphs of the projectile's approach to and impact on the target, as well as the ensuing ejecta and debris clouds. In general, the debris cloud started forming immediately after target perforation. However, the concentration of emerging PE material initially obstructed shadowgraphic light transmission at the target backface until the debris cloud expanded and became "fully developed". For both PEs, this state was typically achieved at $t \approx 100$ µs regardless of v_0, where $t = 0$ denotes projectile impact. High-speed images showing debris cloud development are shown in Figs. S3 and S4. Figure 5 displays high-speed images of fully developed debris clouds resulting from $v_0 \approx 2.5$ km/s HVIs into the UHMWPE (left) and HDPE (right) plates, with initial target temperature increasing sequentially from top to bottom: $T_0 = -120$°C (Fig. 5a and 5b), $T_0 = 23$°C (Fig. 5c and 5d), and $T_0 = 140$°C (Fig. 5e and 5f). In the figures, the UHMWPE (blue) and HDPE (green) targets are sandwiched within the various target assemblies. These assemblies were positioned slightly uprange within the camera's field of view (FOV) to better capture the debris cloud's defining features. Each image displays a scaled projectile icon on the target's uprange side to indicate the direction of impactor motion. In some experiments, the thermocouple wire was visible in the camera's FOV but was far enough from the impact axis to not affect the experiments.

For the $v_0 \approx 2.5$ km/s impacts, both PEs underwent comparable adiabatic shock heating at each T_0 due to their similar densities and heat capacities, and each target's local internal energy surpassed the threshold necessary to fully melt the material (see Section S6). Regardless of T_0,

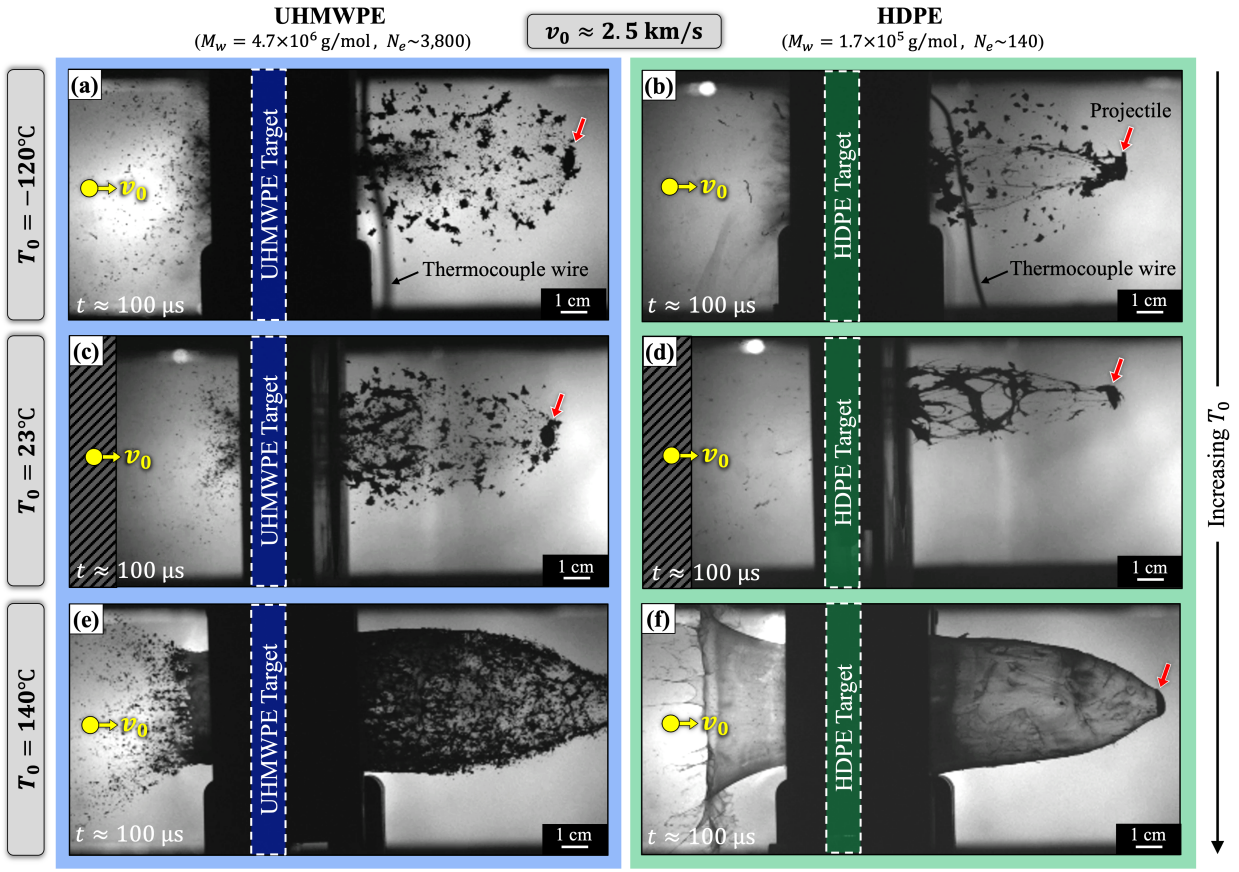

Figure 5: Fully developed HVI debris clouds for UHMWPE and HDPE impacted at $v_0 \approx 2.5$ km/s for temperatures (a, b) $T_0 = -120$°C, (c, d) $T_0 = 23$°C, and (e, f) $T_0 = 140$°C. At $T_0 < T_g$, HDPE shows bulk fragmentation (b) similar to UHMWPE at room temperature (c). At $T_0 > T_m$, UHMWPE's melt response increases (e), aligning its debris cloud geometry closer to that of HDPE (f). Times t are given relative to impact. More debris cloud development is shown in Fig. S3.

after perforation the projectile appeared to be deformed/eroded but largely intact, leading its debris cloud. For the UHMWPE plate, lowering its temperature below T_g resulted in significant target brittleness, with a large number of small particles in the debris cloud (Fig. 5a). This low target temperature ($T_0 = -120$°C) further restricted the UHMWPE polymer chains' freedom to move relative to one another while undergoing rapid deformation beyond the constraint already imposed by their extremely entangled molecular network ($N_e \sim 3,800$). Consequently, the increased molecular relaxation times caused local stresses to spike, resulting in pronounced brittle fragmentation behavior, even as impact-induced temperatures exceeded the melting temperature T_m (*cf.* Fig. S5). For the same T_0, HDPE displayed a similar quasi-brittle fragmentation response, with the exception of a minor amount of melted material around and trailing the deformed projectile (Fig. 5b). This molten material likely experienced a temperature rise sufficient to overcome the effective chain

immobilization caused by its entanglements and depressed T_0 value. The low-temperature PEs' fully developed debris cloud envelopes were each traced and then superimposed to underscore their similarities at this T_0 value (Fig. 6a). These key observations strongly support the conclusion by Rogers *et al.* (*22*) that the major differences in the PEs' HVI responses *at room temperature* stemmed from an interplay between the rate of loading and the average rate of molecular disentanglement and reorientation. In essence, lowering T_0 for fixed N_e inhibited high-rate chain motion analogously to increasing N_e at fixed T_0, making HDPE behave more like UHMWPE when subjected to similar HVIs (more later). At room temperature, UHMWPE and HDPE showed the "bulk fragmentation" and "bulk melting" behavior (Fig. 5c and 5d), respectively, reported in Ref. (*22*) (*cf.* Fig. 1). This consistency underscores the repeatability of the PEs' HVI responses, even with a nearly threefold increase in h_t/d_p. As an aside, changing the material manufacturer also does not appear to affect the ultra-high-rate response of each PE at room temperature (*cf.* (*55*)). The PEs' dynamic failure behavior differed the most at this 23°C T_0 value, leading to pronounced differences in fully developed debris cloud expansion behavior (Fig. 6c).

For $T_0 > T_m$ and $v_0 \approx 2.5$ km/s, the UHMWPE target's debris cloud was more elongated along the impact axis and denser in appearance due to an increased presence of apparent interconnected material (Fig. 5e). This shift in bulk HVI response at this higher (140°C) target temperature is also attributable to the enhanced available molecular motion, which decreases as temperature drops. Increasing T_0 above T_m substantially enhanced free volume, increased rates of disentanglement and reorientation, and shortened relaxation times for the long PE chains. The impact-induced shocks and rapid visco-plastic deformation elevated local temperatures well beyond T_m, further amplifying molecular motion (*cf.* Fig. S5). As a result, the molten UHMWPE in the nascent debris cloud flowed readily during early expansion. However, the amorphous polymer network remained extremely entangled and constrained. As the hot expanding material stretched and thinned, it experienced some disentanglement and cooled. The extremely long PE molecules undergoing rapid deformation became increasingly immobile. Instantaneous rates of disentanglement and reorientation dropped and relaxation times spiked. At some critical level of material expansion, the polymer chains could no longer disentangle and/or reorient to relax the rapidly rising stresses. Stress accumulation then gave way to chain scission. Macroscopically, the highly viscous liquid ceased to flow and fractured rather uniformly, producing a dense cloud of UHMWPE fragments.

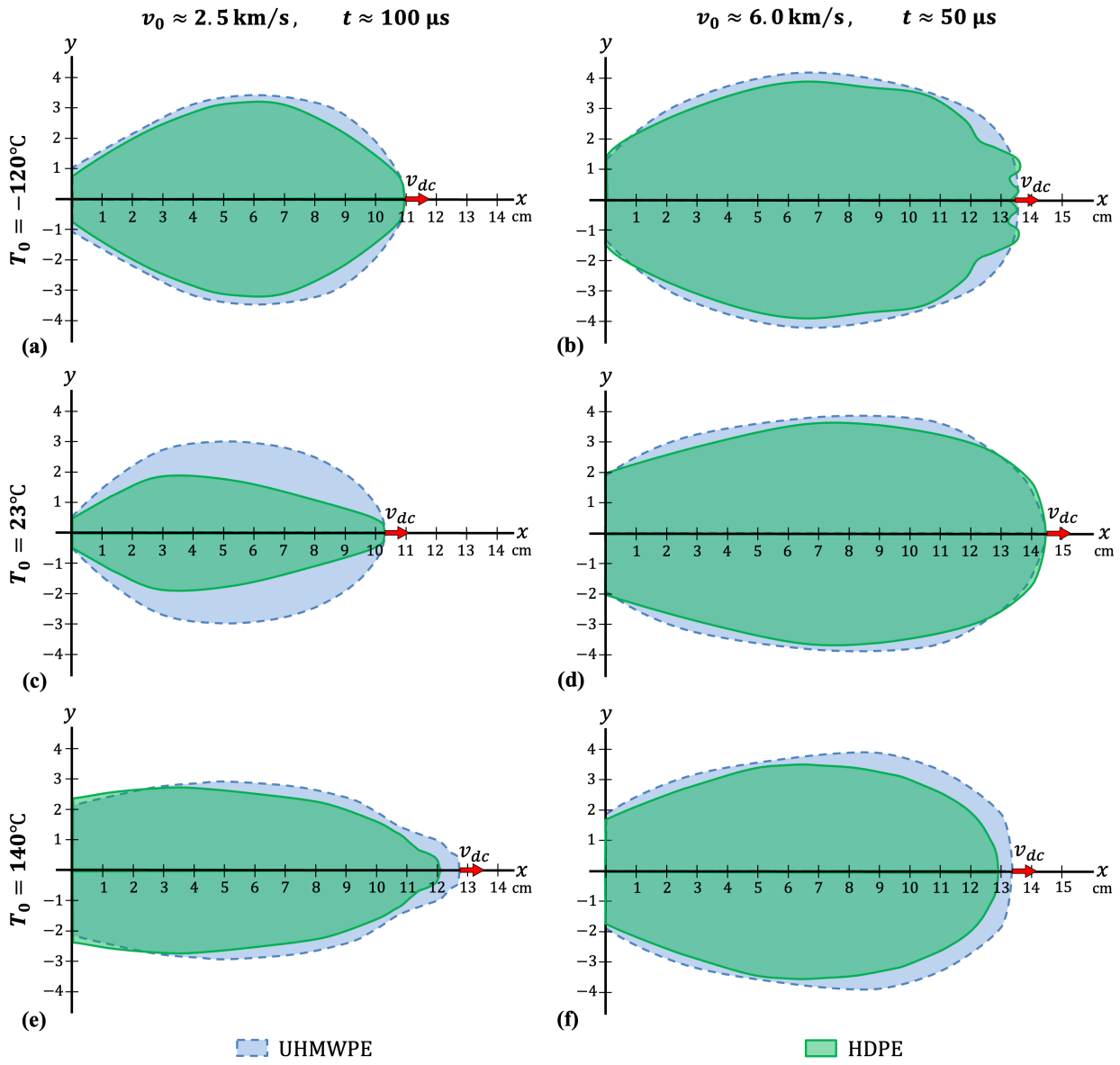

Figure 6: Superimposed HVI debris cloud envelopes for UHMWPE and HDPE at specific temperatures (rows) and impact velocities (columns), with times t given relative to impact. At $T_0 = 23$°C and $v_0 \approx 2.5$ km/s (c), debris cloud shapes differ significantly, but at $T_0 = -120$°C and $T_0 = 140$°C, they are similar, indicating comparable failure modes and expansion rates at these transition temperatures. At $v_0 \approx 6.0$ km/s, debris cloud geometries and expansion rates are alike across all T_0, showing that temperature sensitivity diminishes as strain rate increases.

The quasi-brittle HVI responses of room temperature UHMWPE and $T_0 < T_g$ HDPE were also attributed in part to this failure process; however, material fracture occurred prior to such extensive flow, creating noticeably less dense, interconnected, and elongated debris clouds.

A more extreme case of UHMWPE's dynamic failure process explains the characteristic web-like structure seen in the room temperature HDPE target debris cloud (*cf.* Fig. 5d). Initially, this

debris cloud resembled a thick, rapidly expanding membrane or "bubble" of continuous molten material. The thickness of this membrane, however, was nonuniform. As expansion continued, its thinner regions experienced disproportionately more biaxial strain, forcing the deforming HDPE chains to disentangle, reorient, and relax in the flow directions faster than those in the thicker regions. Some molecules perhaps even became sufficiently aligned in the strain directions to form strain-induced crystalline domains (*76*). Relative chain motion in the more quickly rearranging chains decreased until the thinning bulk material could no longer sustain flow and elongation. Stresses within the local polymer network increased until chain scission occurred. Macroscopically, the membrane material in the thinner regions ruptured and subsequently retracted into the thicker regions as in-plane stresses relaxed. Elongated PE chains returned to more entropically favored conformations, and the average distance between chain ends dropped. Following this rupture process, the thicker regions elongated and formed an expanding network of interconnected molten HDPE fibrils.

Given that both PEs were subjected to similar loading conditions ($v_0 \approx 2.5$ km/s), the difference in their fragmentation/rupture thresholds at a given T_0 value is largely due to the drastic difference in their average number of entanglements (*i.e.*, UHMWPE is ~2,600% more entangled that HDPE).[3] Experimental observations support this interpretation. For HDPE heated above its T_m, the increased free volume enabled its shorter, less entangled chains to become highly mobile. Adiabatic heating from shocks and rapid visco-plastic deformation further enhanced this molecular mobility to levels sufficient for bulk material flow at extremely high impact loading rates ($\dot{\varepsilon} \sim 10^6$ s^{-1}). This shift in microstructural response time facilitated the formation of a membrane-like debris cloud that could sustain remarkable levels of expansion without rupturing (Fig. 5f). Hence, HDPE's debris cloud expansion threshold was significantly extended by a T_0-induced increase in chain mobility. In addition, the HVI-induced debris clouds for the UHMWPE and HDPE targets at $T_0 > T_m$ were similar (Fig. 6e). These findings strongly suggest that rising T_0 increasingly aligns UHMWPE's HVI behavior with HDPE's. Furthermore, decreasing T_0 brings HDPE's response closer to UHMWPE's, provided that v_0 is fixed. For both PEs, the degree of debris cloud expansion at which material breakup begins primarily determined the size and shape of debris cloud fragments/fibrils and the

[3]For the PE plates heated to $T_0 > T_m$, most of the crystalline regions in the semi-crystalline PEs were melted and converted to amorphous arrangements. This suggests that both PEs in the following discussion were both amorphous networks of entangled PE molecules, primarily differing in M_w and N_e.

level of apparent material connectivity. This threshold is governed by the average rate at which neighboring chains can disentangle and reorient, which depends largely on T_0, v_0, and N_e.

Increasing the impact velocity to $v_0 \approx 6.0$ km/s shortened the perforation event duration by roughly 60%, which in turn raised both the heating and loading rates experienced by the deforming PE material. As a result, local target temperatures well exceeded T_m for both PEs regardless of T_0, and strain rates reached 10^7 s^{-1} (*cf.* Fig. S5). These changes to the temporal and spatial distributions of temperature and strain rate undoubtedly altered the predominant energy absorption mechanisms and dynamic failure behaviors for both PEs. High-speed images of debris clouds resulting from $v_0 \approx 6.0$ km/s HVIs on the roughly −120°C, 23°C, and 140°C PE plates are shown in Fig. 7, which is arranged similarly to Fig. 5. At $T_0 = -120$°C, UHMWPE's debris cloud consisted of discrete, irregularly shaped fragments of varying size (Fig. 7a), consistent with findings at $v_0 \approx 2.5$ km/s (*cf.* Fig. 5a). The significant fragmentation seen for HDPE at $v_0 \approx 2.5$ km/s and $T_0 < T_g$ was partially reversed at the higher velocity, as the more severe impact-induced heating facilitated more instantaneous chain mobility. Instead, HDPE's debris cloud featured disconnected, elongated fragments (Fig. 7b), shaped by the process that formed its ruptured and unruptured membrane structures at $T_0 = 23$°C and $T_0 = 140$°C, respectively (*cf.* Figs. 5d and 5f). Yet, when $T_0 = -120$°C, impact-induced heating could not raise the target temperature enough to facilitate the same degree of chain elongation, separation, or disentanglement on the time scale of the strain. Hence, the HDPE molecules became effectively frozen within the rapidly stretching fibrils, causing them to fracture prematurely at necking regions during elongation.

At room temperature, the debris clouds for the UHMWPE and HDPE plates impacted at $v_0 \approx 6.0$ km/s exhibited bulk fragmentation (Figs. 7c) and bulk melting (Fig. 7d) responses, respectively, that were virtually indistinguishable from those reported in Ref. (*22*) (*cf.* Fig. 1). At $T_0 = 140$°C, the UHMWPE debris cloud contained more molten material, as indicated by the presence of a dense web-like structure in its uprange portion, where expansion rates were lowest (Fig. 7e). The HDPE plate impacted under similar conditions displayed a continuous membrane-like debris cloud of molten material that withstood much greater levels of expansion without rupturing (Fig. 7f), similar to observations at $v_0 \approx 2.5$ km/s for the same T_0 (*cf.* Fig. 5e). Both PEs' debris clouds densified with rising temperatures, featuring fewer distinct fragments/fibrils and more continuous material. This finding further emphasizes that, at a constant v_0, a higher T_0 increased

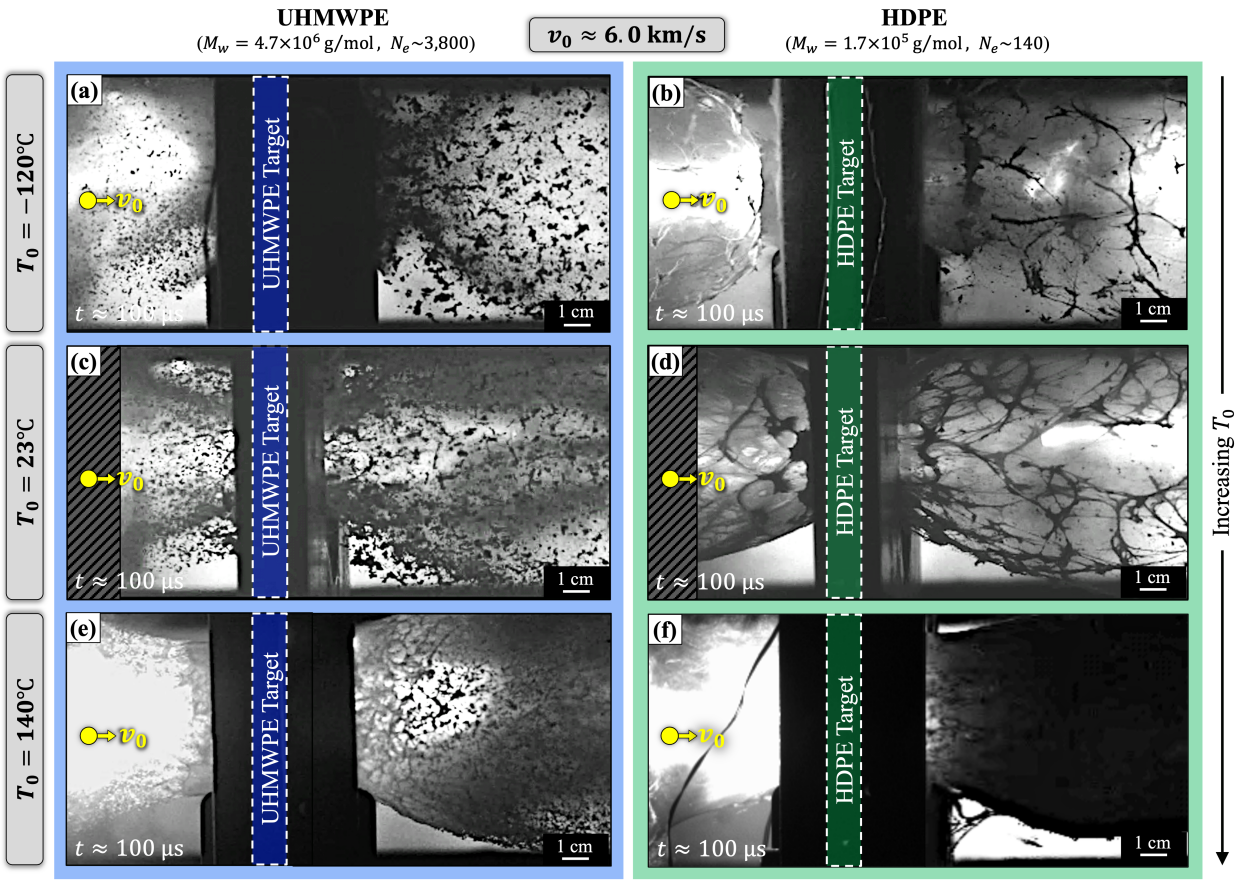

Figure 7: Fully developed HVI debris clouds for UHMWPE and HDPE impacted at $v_0 \approx 6.0$ km/s for temperatures (a, b) $T_0 = -120$°C, (c, d) $T_0 = 23$°C, and (e, f) $T_0 = 140$°C. The fraction of melted material in the UHMWPE debris cloud increases with rising T_0 (a, c, e), despite concurrent bulk fragmentation at a given degree of debris cloud expansion (e). Conversely, melting in HDPE decreases below $T_0 < T_g$, although it remains present (b). These findings indicate that the bulk behavior of the PEs is influenced by a competition between temperature, strain rate, and disentanglement rate (chain mobility). Times t are given relative to impact. More debris cloud development is shown in Fig. S4.

the expansion threshold at which debris cloud fragmentation/rupture began due to added chain mobility (*i.e.*, higher rates of disentanglement/reorientation and thus shorter relaxation times). At $v_0 \approx 6.0$ km/s for all T_0 values, both PEs showed similar debris cloud geometries and expansion rates, indicating reduced temperature sensitivity at higher loading rates.

The considerable alterations in PE molecular mobility, caused by cooling and heating the targets pre-impact, likewise resulted in significant variations in their deformation and failure features observed post-impact. For the −120°C UHMWPE plate impacted at $v_0 \approx 2.5$ km/s, the perforation diameter was only marginally larger than that of the impactor (Fig. 8a). Residual out-of-plane deformation was present on both target faces but most prominent on the back side (Fig. 8b). Radial, circumferential, and in-plane target cracks nucleated but were quickly arrested, resulting

in a jagged and rough failure surface akin to those seen in similar room temperature samples in Ref. (*22*). UHMWPE's quasi-brittle failure was thus mainly localized to the material in contact with and immediately surrounding the projectile during target perforation. The resulting fragments ultimately populated its debris cloud (*cf.* Fig. 5a). The absence of extensive radial or circumferential cracking underscores UHMWPE's strong resistance to crack propagation even when subjected to HVI near its T_g. Impact-induced stress waves, however, interacted to focus extreme tensile stresses on an inclined conical plane encircling the impact site. These stresses readily surpassed the material's dynamic strength, causing voids to nucleate. These voids coalesced into a large cone-shaped fracture surface (*i.e.*, "cone crack"), akin to that observed in impacted brittle materials (*77*). The spalled material, lacking enough residual momentum and energy for complete ejection, formed a raised circular region on the target's back side (Fig. 8b).

The $T_0 = -120°$C HDPE target, impacted at the same $v_0 \approx 2.5$ km/s, showed widespread radial, circumferential, and in-plane cracks (Fig. 8c and 8d). With $T_0 < T_g$, the crystalline regions in the highly crystalline HDPE target could not melt in the impact event's time frame. As HDPE lacked UHMWPE's densely entangled molecular network to facilitate load transfer, stresses concentrated in these regions until they effectively shattered, leading to pronounced brittle failure of the bulk material. The perforation diameter for the HDPE target was almost double that of the projectile. The extreme adiabatic heating during impact softened/melted the material directly around the projectile, resulting in flow patterns on the perforation surface. These features were localized to the inner walls of the opening, as HDPE's poor thermal conductivity inhibited the lateral heating needed to enable any additional material ductility and/or flow. This observation explains the relatively small amount of melted HDPE trailing the deformed projectile in the high-speed images (*cf.* Fig. 5b). There was minimal out-of-plane deformation on either side of the target. Spalled and ejected material from the target's back side, however, left behind a conical indentation concentric with the perforation (Fig. 8d).

The perforation characteristics for the room temperature PE plates impacted at $v_0 \approx 2.5$ were consistent with those observed in Ref. (*22*). The effective perforation diameter for the UHMWPE target was slightly smaller than that for the HDPE target (Fig. 8e–8h). The opening in each target was smaller in size than its respective counterpart at the lower T_0 value (*cf.* Fig. 8a–8d). For both 23°C PE plates, the impact-induced deformation morphology and failure features were more localized

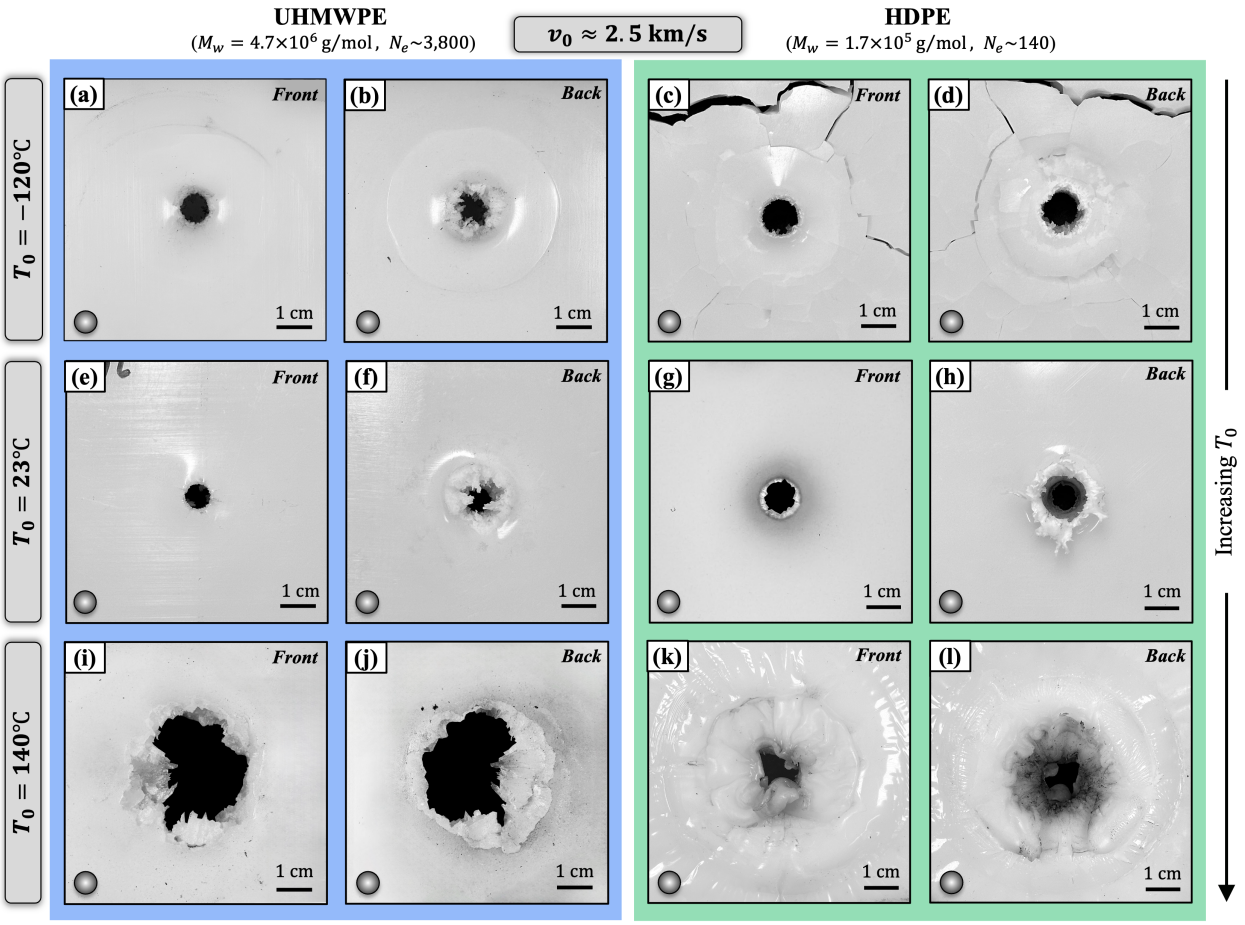

Figure 8: Front and back side images of UHMWPE (left) and HDPE (right) target perforations resulting from HVIs at $v_0 \approx 2.5$ km/s across target temperatures: (a–d) $T_0 = -120$°C, (e–h) $T_0 = 23$°C, and (i–l) $T_0 = 140$°C. For both PEs, perforation diameters (d_e) were smallest at room temperature (e–h) and notably increased at $T_0 > T_m$ (c, d, k, l). Residual out-of-plane deformation was also most pronounced for both materials at this T_0. UHMWPE resisted crack propagation and flow at each T_0, while HDPE exhibited extensive brittle fracture (radial, circumferential, and in-plane cracking) at $T_0 < T_g$ (c, d) and flow at $T_0 > T_m$ (k, l). A projectile is superimposed on each image for scale.

around the perforation. For example, the cone crack and raised circular region were now missing from the UHMWPE target's back side. Yet, its failure surfaces remained jagged and rough. The comparable HDPE plate showed significant residual out-of-plane deformation on the rear side (Fig. 8h), suggesting extensive impact-induced material softening/melt and flow. Notably, finger-like protrusions on the circumferential rim surrounding the perforation indicated former attachment points of molten drawn HDPE fibrils seen in the high-speed images (*cf.* Fig. 5d).

Heating the targets to $T_0 = 140$°C drastically changed the perforations for the same $v_0 \approx 2.5$ km/s. The molten UHMWPE target showed a more jagged, asymmetrical perforation (Fig. 8i and 8j), with its effective diameter increasing by nearly 280% compared to that at room temperature

(Fig. 8e and 8f). Virtually no cracks or out-of-plane deformation surrounded the perforation on either target side, and failure surfaces showed minimal signs of melting and flow. Extreme adiabatic heating from impact-induced shocks and rapid plastic deformation raised the target temperature to levels were some material flow was possible, as observed in the early stages of debris cloud expansion (*cf.* Fig. S3i). However, PE's poor thermal conductivity limited this flow to heated material near and along the impact axis. Target material further (radially) from the impact axis did not experience this temperature rise but still experienced considerable strains, strain rates, and stresses. In these peripheral regions, UHMWPE's molten, but still highly entangled, molecular network lacked the mobility necessary to flow on the time scale of the strain. As the opening expanded radially due to residual momentum and energy in the target material, the highly viscous liquid PE resisted flow, experienced intense stress, and succumbed to melt fracture (*78*). Warming the HDPE target dramatically suppressed its viscosity, leading to an increased susceptibility for bulk softening and flow. Consequently, its deformation morphology and failure surfaces differed markedly from those observed at the lower T_0 values. For example, the material around the perforation appeared to have been significantly stretched before elastically recovering/retracting post-impact (Fig. 8k). This process produced a target opening with an effective diameter virtually no larger than that seen for the room temperature sample. Significant charring/discoloration present on the failure surface (Fig. 8l) indicated that the impact elevated local target temperatures enough to activate HDPE's thermal degradation, consistent with numerical predictions (*cf.* Fig. S5). Some visco-plastic deformation from stress waves traveling through the target rippled its once flat surfaces. Even so, the elastic recovery of the material in the perforation region minimized residual out-of-plane deformation.

The PE targets experienced significantly more catastrophic failure when impacted at $v_0 \approx 6.0$ km/s, independent of T_0. Yet, altering T_0 at this velocity did lead to notable variations in the primary deformation and failure mechanisms exhibited by each PE. For instance, the -120°C UHMWPE plate showed a perforation roughly eight times larger in diameter than the impactor (Fig. 9a) and five times larger in diameter than that seen for the comparable target impacted at $v_0 \approx 2.5$ km/s (*cf.* Fig. 8a). The morphology of the irregular perforation surface clearly suggested UHMWPE brittle fracture, and residual out-of-plane deformation was virtually nonexistent. A cone-shaped fracture surface, showing signs of extensive charring/discoloration indicative of PE thermal degradation, formed around the perimeter of the opening (Fig. 9b). A large ring-shaped

spall fragment, akin to the one not fully detached from the cold target impacted at $v_0 \approx 2.5$ km/s, was ejected following the primary HVI event (*cf.* Fig. S6). At the amplified impact-induced strain rates, UHMWPE's highly entangled microstructure struggled to evenly distributed sharply rising stresses, and the target succumbed to some radial and in-plane cracking. For the same T_0, the HDPE plate exhibited an effective perforation diameter similar to that for the −120°C UHMWPE target. However, the HDPE plate's target opening had a notably more jagged and non-circular perimeter (Fig. 9c and 9d). The fracture surfaces defining the perforation wall also showed evidence of PE thermal degradation. Extensive radial, circumferential, and in-plane cracking effectively shattered the embrittled HDPE plate during and immediately after impact. Consequently, the plate was kept in the fixture for post-impact perforation imaging, and the fragments were collected and imaged once removed from the fixture (*cf.* Fig. S7).

The predominant deformation and failure features observed for each room temperature PE target impacted at $v_0 \approx 2.5$ km/s did not appear to change when v_0 was increased to 6.0 km/s. In addition, they continued to align with those from similar HVI experiments presented in Ref. (*22*). However, the faster perforation event at $T_0 = 23$°C resulted in much more severe out-of-plane deformation for both PE targets, especially on their front faces (Figs. 9e–9h). The ∼150% increase in v_0 resulted in a 200% and 236% increase in effective perforation diameter for the $T_0 = 23$°C UHMWPE and HDPE targets, respectively. The fracture surfaces originally seen in the UHMWPE sample impacted at $v_0 \approx 2.5$ km/s were even more apparent at the higher velocity. The opening's in-plane perimeter was highly irregular due to short radial cracks, and stunted in-plane cracks caused the surrounding material to fan out perpendicularly. Together, these cracks formed a perforation wall with a distinctive peak-and-valley morphology (Fig. 9e and 9f). Conversely, the HDPE target impacted at $v_0 \approx 6.0$ km/s displayed smooth perforation surfaces with clear signs of material softening, melting, and flow at 23°C (Fig. 9g and 9h). The finger-like protrusions that were noticeable on the back surface of the room temperature target impacted at $v_0 \approx 2.5$ km/s became more defined and were also present on the impact side. Material thermal degradation was evident along the inner surface(s) of the opening for both PEs. On its front side, the HDPE target also showed signs of thermal degradation along the rim of out-of-plane deformation that surrounded the perforation (Fig. 9g).

Elevating the PE targets' temperature to $T_0 = 140$°C again significantly altered their perforation

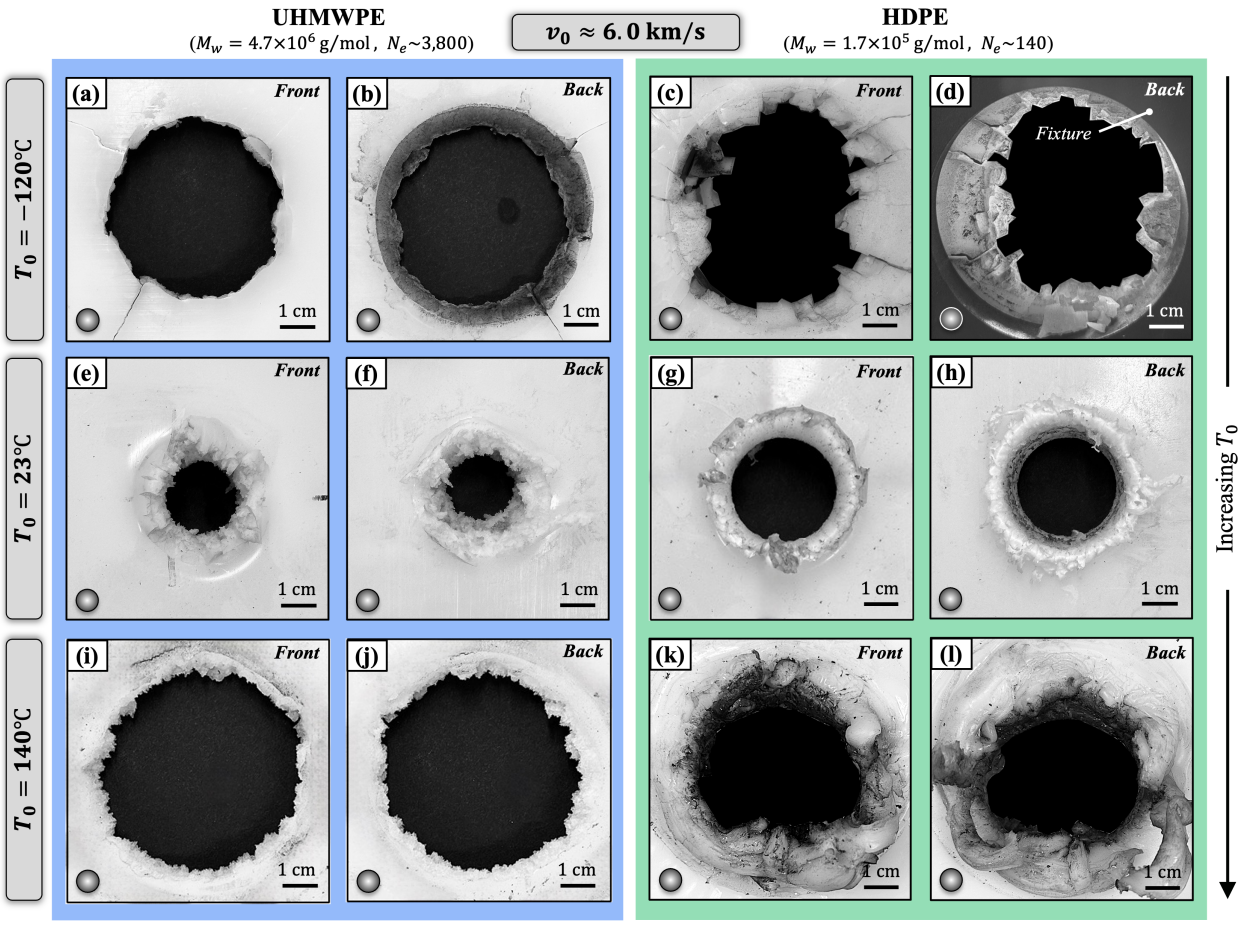

Figure 9: Front and back side images of UHMWPE and HDPE target perforations resulting from HVIs at $v_0 \approx 6.0$ km/s across target temperatures: (a–d) $T_0 = -120$°C, (e–h) $T_0 = 23$°C, and (i–l) $T_0 = 140$°C. At $T_0 = -120$°C, UHMWPE still resisted crack propagation, while HDPE exhibited bulk brittle fracture. For the sample in (a, b), a cone fracture surface formed on the exit side, and a large annular fragment was later ejected (Fig. S6). The HDPE sample in (c, d) completely shattered and was thus photographed before removal from the fixture to prevent it from disassembling (Fig. S7). Extensive material flow, as well as charring (thermal degradation), were evident for the HDPE target at $T_0 = 140$°C (k, l). Out-of-plane deformation was most pronounced for both PEs at room temperature. A projectile is superimposed on each image for scale.

morphologies when impacted at $v_0 \approx 6.0$ km/s. Despite T_0 exceeding T_m, the UHWMPE plate still exhibited jagged, brittle-like fracture surfaces that lined the perimeter of the perforation (Fig. 9i and 9j), which was 170% larger in effective diameter than that of the 23°C target impacted at the same v_0 (Fig. 9e and 9f). Any signs of the molten, flowing material visible in the high-speed images (*cf.* Fig. S4i) were erased/removed as the perforation expanded due to residual momentum and energy in the surrounding target material (residual hole enlargment). At some degree of UHMWPE hole enlargement, the cooler, yet molten, encircling material ceased flowing and started to experience melt fracture, mirroring the behavior seen in the 140°C target impacted at 2.5 km/s

(*cf.* Fig. 8i and 8j). This was not the case for the 140°C HDPE target impacted at 6.0 km/s. Instead, its perforation was encircled by material that had undergone extensive flow, elongation/stretching, fracture/puncture, and elastic recovery (Fig. 9k and 9l). This HDPE deformation and failure resulted in an asymmetrical perforation roughly 30% smaller than that seen in the 140°C UHMWPE plate impacted at the same v_0 (*cf.* Fig. 9i). The HDPE perforation was encircled by finger-like protrusions, which were fewer in number but larger in diameter than those seen on comparable targets impacted at lower T_0. Failed target surfaces for both PEs appeared significantly charred, indicating some material pyrolysis and combustion had occurred.

The perforated plates were also inspected *quantitatively* to better characterize and understand the differences in their HVI-induced responses. The mass of each PE target was measured before and after impact to determine its normalized mass loss ($\Delta m_t/m_p$). For both PEs across all T_0, these values increased with impact velocity ($\Delta m_t/m_p \propto v_0$). At $v_0 \approx 2.5$ km/s, the $\Delta m_t/m_p$ values for UHMWPE showed a monotonic increase with T_0, rising nearly thirtyfold from −120°C to 140°C (Fig. 10a). This trend, however, did not hold for $v_0 \approx 6.0$ km/s. Instead, the 23°C UHMWPE target lost ~80–85% less mass than the −120°C and 140°C plates. This transition underscores the intricate interplay of T_0, v_0, and molecular mobility on dynamic material behavior/failure. In essence, lowering T_0 does make PE more brittle but simultaneously decreases the fraction of material undergoing visco-plastic flow during perforation. UHMWPE's flow, elongation, cooling, and ultimate fracture *is* what primarily drives its fragmentation. At $v_0 \approx 2.5$ km/s, decreasing T_0 suppressed UHMWPE flow without inducing additional fracture/fragmentation, enabling a consistent reduction in $\Delta m_t/m_p$. Conversely, the 6.0 km/s impact into the −120°C UHMWPE target *did* cause more material to fracture, and the resulting fragments (including the spall fragment) together had sixty times more mass than that ejected from the −120°C target impacted at the lower velocity (*cf.* Figs. 9a and 9b). At $T_0 = 140$°C, the UHMWPE target's mass loss was maximized for both v_0, as increased bulk material flow gave way to extensive melt fracture (*cf.* Figs. 9i and 9j). These results show that the degree to which a PE target will fracture/fragment (*i.e.*, lose mass) as T_0 and/or v_0 vary is largely governed by the proportion of its material that can simultaneously resist flow and retain toughness. Hence, at a given combination of v_0 and T_0, the PE plate exhibiting the highest level of combined bulk flow and quasi-brittle fragmentation loses the greatest mass (*e.g.*, the UHMWPE plates at $T_0 = 140$°C).

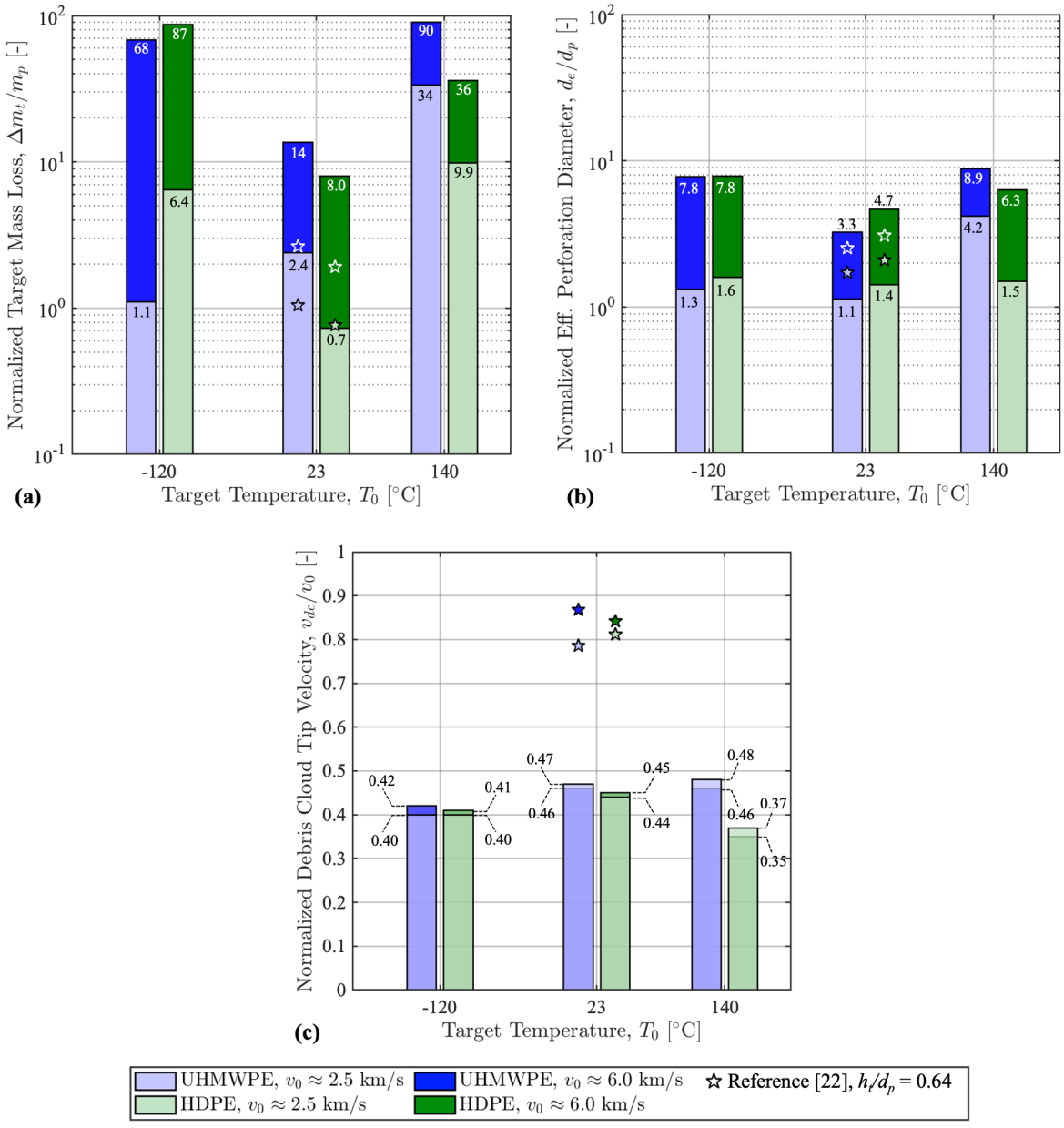

Figure 10: Response of UHMWPE and HDPE plates to HVIs at $v_0 \approx 2.5$ km/s and 6.0 km/s and $T_0 = -120$°C, 23°C, and 140°C: normalized (a) mass loss, $\Delta m_t/m_p$; (b) effective perforation diameter, d_e/d_p; and (c) debris cloud tip velocity, v_{dc}/v_0. For a given PE, $\Delta m_t/m_p$ was greater at the transition temperatures, expect for UHMWPE at $v_0 \approx 2.5$ km/s and $T_0 = -120$°C (a). d_e/d_p (b) also increased at $T_0 = -120$°C and 140°C. v_{dc}/v_0 nominally increased with T_0, expect for the case of HDPE at $T_0 = 140$°C. Data reported in Ref. (*22*) for $h_t/d_p = 0.64$ is included for reference.

This finding also aligns with the HVI response of the HDPE targets. At $T_0 = -120$°C, both HDPE targets experienced widespread brittle fracture (cracking), leading to 80–100% more mass loss than its room temperature samples (*cf.* Figs. 8c, 8d, 9c, 9d). The 140°C HDPE targets likewise

experienced more mass loss but due to extensive visco-plastic flow, elongation, and moderate fracture (*cf.* Figs. 8k, 8l, 9k, 9l). These T_0-induced transitions in HDPE's HVI response resulted in trough-shaped $\Delta m_t/m_p$ *vs.* T_0 trends for both v_0 (Fig. 10a). All 23°C and 140°C HDPE targets, experiencing primarily thermal softening/melting and flow, consistently lost less mass than the comparable UHMWPE targets, consistent with findings from Ref. (*22*). However, this relationship was reversed at $T_0 = -120$°C due to HDPE embrittling more than UHMWPE. Interestingly, the highest target mass loss value for each PE was achieved at opposite extremes of the T_0 range, with both losing around ninety times the projectile's mass. Comparable data from Ref. (*22*) (h_t/d_p = 0.64, m_p = 1.41 g) is also displayed on the plot for comparison.

Perforations were also compared across experiments using their normalized effective diameter ratios (d_e/d_p). In general, d_e/d_p increased with impact velocity. For each v_0, the perforations in the −120°C and 23°C HDPE targets were larger than those in the similar UHMWPE targets (Fig. 10b), a trend consistent with findings reported in Ref. (*22*). However, at T_0 = 140°C, the UHMWPE targets had larger d_e/d_p values, as they underwent substantial post-impact residual hole enlargement *via* melt fracture (*cf.* Figs. 8i and 9i). Such hole enlargement was suppressed in the hot HDPE melted plates due to the material elastic recovery/retraction that occurred post-perforation (*cf.* Figs. 8k and 9k). The HDPE targets impacted at 2.5 km/s showed no significant change in d_e/d_p with varying T_0, though there were some variations at $v_0 \approx 6.0$ km/s. At room temperature, the HDPE targets showed larger d_e/d_p values but less mass loss compared to the UHMWPE targets because of HDPE's capacity for large-scale plastic deformation, as opposed to UHMWPE's tendency to fragment (*cf.* Fig. 10a). At $T_0 = -120$°C and 140°C, larger perforation diameters were associated with greater mass loss values for both PEs regardless of v_0, a change attributed to HDPE's distinct deformation behaviors and failure mechanisms at the extreme temperatures.

Analyzing the high-speed *in-situ* images of each HVI event offered insight into the PE targets' relative degrees of energy absorption. For each experiment, the debris cloud's downrange-most tip was tracked over time (along the impact axis) to calculate its average velocity (v_{dc}). The variations in the v_{dc} measurements, caused by the camera's pixel resolution, were approximately ±0.05 km/s. This velocity was then normalized by the corresponding v_0 for comparison with the other experiments. The v_{dc}/v_0 values for the UHMWPE targets impacted at 2.5 km/s increased by 15–20% from $T_0 = -120$°C to $T_0 = 140$°C ($v_{dc}/v_0 \propto T_0$; Fig. 10c). A similar increase was

seen between the −120°C and 140°C UHMWPE targets impact at 6.0 km/s; however, there was virtually no change in v_{dc}/v_0 from T_0 = 23°C to T_0 = 140°C. The normalized tip velocities similarly increased for the −120°C and 23°C HDPE targets. These $v_{dc}/v_0 \propto T_0$ trends align with expectations, as increases in temperature typically reduce material viscosity, hardness, and strength due to enhanced chain mobility. Notably, UHMWPE's densely entangled microstructure fought activation of any new/additional predominant energy dissipation mechanisms as T_0 and v_0 varied. For all T_0, the v_{dc}/v_0 values for the UHMWPE plates were the same as or higher than those for the HDPE targets, a finding that suggests HDPE absorbed more projectile energy [$E_p \propto 1 - (v_{dc}/v_0)^2$]. The normalized tip velocities for the 140°C HDPE plates were notably the lowest among all targets, regardless of v_0 or T_0. In particular, they were about 25% lower than those for the UHMWPE targets heated to the same temperature (Fig. 10c). This reversal in HDPE's trend (*i.e.*, $v_{dc}/v_0 \propto T_0 \rightarrow v_{dc}/v_0 \propto 1/T_0$) suggests that (*i*) there is a shift in its predominant energy dissipation/failure mechanisms, (*ii*) these mechanisms are being engaged for a longer duration of time, or (*iii*) more mechanisms are being activated simultaneously (more later). Comparable debris cloud tip velocity data for the HVI samples in Ref. (*22*) are plotted in Fig. 10c for comparison. *These results strongly suggest that, for a PE target impacted at a given* v_0*, there exists an optimal* T_0 *value or, alternatively, degree of molecular mobility, that maximizes its energy absorption* (E_p).

The pre-impact, *in-situ*, and post-impact findings together affirm that differences in deformation behavior, failure modes, and relative energy absorption between UHMWPE and HDPE can essentially be attributed to molecular mobility. At a constant N_e value, raising the temperature of a given PE target increases its free volume, promotes chain disentanglement and reorientation, and reduces relaxation times. Conversely, increasing N_e at constant T_0 has the opposite effect. When subjected to HVI, a PE target with less constrained chains will experience increased large-scale thermal softening/melting and flow. Under identical impact conditions, imposed constraints on the target's microstructure, either by reduced T_0 or elevated N_e, will induce more pronounced quasi-brittle fragmentation. Increasing v_0 alone can effectively embrittle a target by raising the average strain rate [$\dot{\bar{\varepsilon}} = f(v_0, h_t, d_p, \ldots)$] beyond the rates of disentanglement and reorientation. The target that exhibits the most visco-plastic flow without bulk fragmentation will generally lose less mass, have smaller perforations, and better absorb energy. These observations suggest there is a critical

691 average number of entanglements,

$$N_e^* = f(T_0, v_0, h_t, d_p, \dots) = f(T_0, \dot{\bar{\varepsilon}} \dots), \tag{1}$$

692 that, for fixed v_0, T_0, and projectile-target combination, characterizes a PE target's transition in HVI
693 response from extensive quasi-brittle fragmentation to bulk thermal softening/melting and flow.
694 Hence, the proximity of a target's N_e value to N_e^* is a strong indicator of its ability to absorb energy.
695 In general, the energy absorbed by a target subjected to HVI can be expressed as

$$E_p = \int_0^{\tau} \dot{E}_p(t)\, dt, \tag{2}$$

696 where τ represents the time (relative to impact) at which the projectile (or its fragments) and
697 the target cease to interact, t is the event time, and $\dot{E}_p(t)$ is the target's instantaneous energy
698 dissipation rate. The longer the material remains intact during perforation, the more time energy
699 dissipation mechanisms can operate (*i.e.*, increased τ). Similarly, the more material that stays intact
700 during perforation, the greater the proportion of deforming material that can dissipate energy (*i.e.*,
701 enhanced $\dot{E}_p$).

702 For fixed T_0 and $\dot{\bar{\varepsilon}}$, an impacted PE target will initially dissipate some energy through adiabatic
703 shock heating, light emission, vaporization, and more, regardless of N_e. If $N_e \gg N_e^*$, the target
704 continues to dissipate energy *via* rapid plastic work, thermal degradation, chain scission, and some
705 local fracture before sudden widespread fragmentation of the deforming/flowing material causes
706 a premature drop in $\dot{E}_p$ (Fig. 11a, $E_p^{(a)}$). For $N_e \approx N_e^*$, fragmentation does not occur; instead, the
707 target absorbs more energy due to increased thermal softening/melting and prolonged visco-plastic
708 flow. The expanding material behaves like a membrane, prolonging interaction with the projectile
709 and extending the impact time, τ. As the material expands, it begins to experience rupture and
710 fibrillation, leading to a gradual decrease in the target's instantaneous energy dissipation rate, $\dot{E}_p$,
711 as more material fractures (Fig. 11b, $E_p^{(b)}$). When $N_e \ll N_e^*$, rupture is avoided, and $\dot{E}_p$ remains
712 nonzero while the projectile interacts with the expanding, cooling, and stiffening PE material.
713 Eventually, at a certain τ, the projectile punctures the membrane, ceasing its interaction with the
714 target (Fig. 11c, $E_p^{(c)}$).

715 As $N_e \to 0$ for the same impact conditions, the accompanying reduction in PE viscosity,

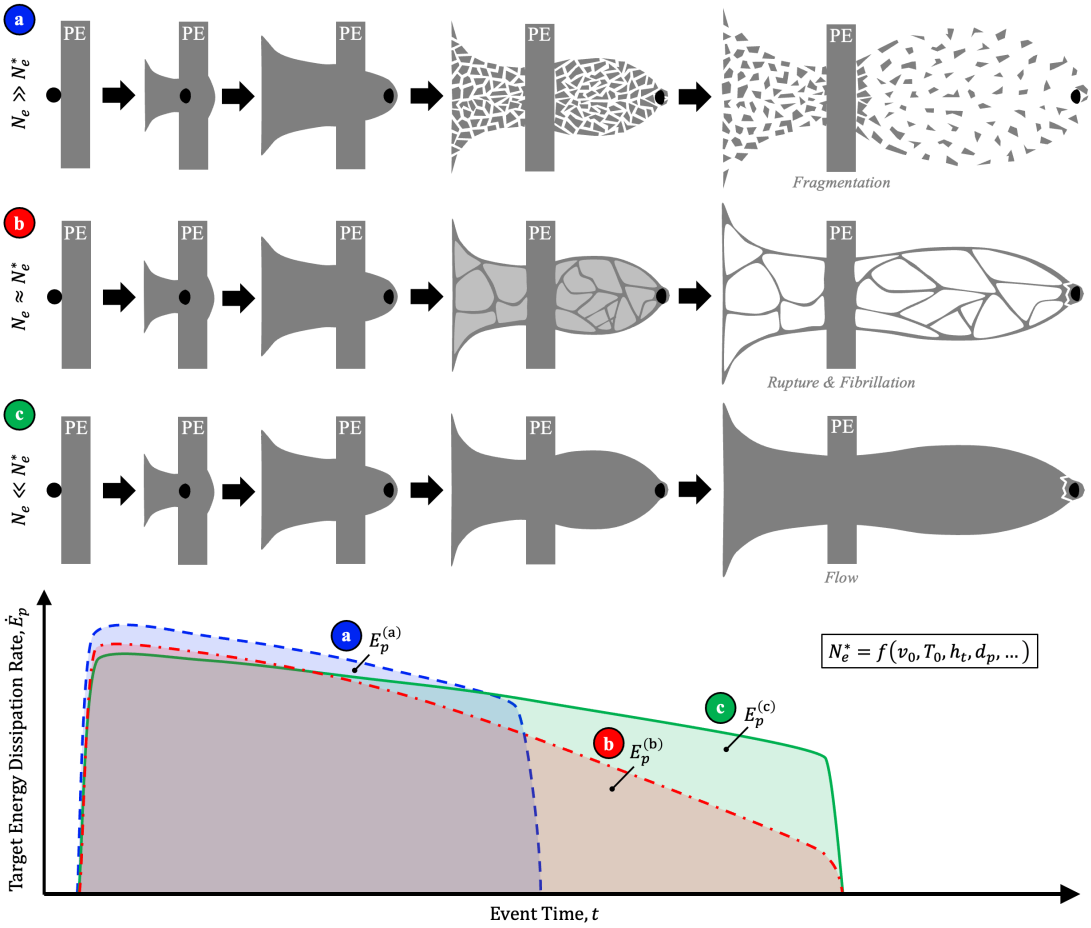

Figure 11: The effect of a PE's average number of entanglements per chain (N_e) on its primary failure modes when subjected to HVI: (a) at $N_e \gg N_e^*$, restricted molecular mobility leads to debris cloud fragmentation; (b) at $N_e \approx N_e^*$, a nonuniform membrane-like debris cloud forms, thins, and ruptures, resulting in an interconnected web-like network of PE fibrils; (c) at $N_e \ll N_e^*$, the decreased restriction on molecular mobility facilitates the formation of a membrane-like structure that can extensively expand without rupturing. The critical average number of entanglements per chain, $N_e^* = f(v_0, T_0, h_t, d_p, \ldots)$, marks the threshold at which the material shifts from predominantly bulk fragmentation to bulk flow. PEs with intermediate N_e values display a mixture of these behaviors. Each bulk material failure mechanism initiates at a different event time, t, leading to variations in target energy absorption, $E_p = \int \dot{E}_p \, dt$, (*i.e.*, failed materials cease to dissipate energy).

strength, toughness, *etc*. begins to negate the improvements in E_p. Thus, there is an optimal N_e value, $\hat{N}_e < N_e^*$, that maximizes E_p. For fixed T_0, a target impacted at $v_0^{(1)}$ will experience an average strain rate of $\dot{\varepsilon}^{(1)}$. The target's energy absorption is maximum ($\max E_p^{(1)}$) when $N_e = \hat{N}_e^{(1)} < N_e^{*(1)}$. Another target of identical geometry impacted by the same projectile at $v_0^{(2)}$ will experience average strain rate $\dot{\varepsilon}^{(2)}$. Its maximum energy absorption value ($\max E_p^{(2)}$) will be achieved at $N_e = \hat{N}_e^{(2)} < N_e^{*(2)}$. If $v_0^{(1)} > v_0^{(2)}$, then $\dot{\varepsilon}^{(1)} > \dot{\varepsilon}^{(2)}$ and $\hat{N}_e^{(1)} < \hat{N}_e^{(2)}$ (Fig. 12a and 12b). This $\hat{N}_e \propto 1/\dot{\varepsilon}$ relationship is analogous to the time-temperature superposition principle exhibited by

PE. In essence, increasing average strain rate requires a reduction in N_e to sustain the degree of molecular mobility that leads to maximum E_p (Fig. 12c). Since T_0 increases molecular mobility, $\hat{N}_e \propto T_0$. This finding demonstrates the feasibility of a layered protective structure composed of $\mathcal{N}$ monolithic PE plates that is optimized for a specific impact threat envelope (*i.e.*, ranges of v_0, d_p, m_p, *etc.*). Given an envelope, N_e of the i-th plate ($i = 1, 2, 3, \ldots, \mathcal{N}$) would be tuned to the optimal value ($\hat{N}_e^{(i)}$) specific to the local anticipated average strain rate ($\dot{\bar{\varepsilon}}^{(i)}$). Assuming the projectile impacts the $i = 1$ plate, $\dot{\bar{\varepsilon}}^{(i)}$ will decrease and $\hat{N}_e^{(i)}$ will increase as i increases (Fig. 12d). In this way, each PE layer is designed for optimal energy absorption.

4 Conclusions

The declining efficacy of traditional spacecraft MMOD shields and military ballistic armor necessitates the development of layered, threat-optimized protective structures for HVI mitigation. UHMWPE and HDPE show promise as intermediate layers, owing to their high mass-specific energy absorption, tailorability, and low density and cost. While the relatively low-rate ($\dot{\varepsilon} < 10^3$ s^{-1}) behaviors of these PEs are well-documented, their responses to HVI-induced strain rates ($\dot{\varepsilon} > 10^6$ s^{-1}) are virtually unexplored and not well understood, especially near their T_g and T_m values. This study investigated the interplay of T_0, v_0, and N_e on PE's HVI response to help address fundamental questions about its dynamic behavior and highlight its engineering applications. 12.7 mm thick UHMWPE ($M_w = 4.7 \times 10^6$ g/mol, $N_e \sim 3,800$) and HDPE ($M_w = 1.7 \times 10^5$ g/mol, $N_e \sim 140$) plates were subjected to 2.5 km/s and 6.0 km/s HVIs by 6.35 mm diameter 2017-T4 aluminum spheres. Targets were impacted at $T_0 = -120$°C, 23°C, and 140°C.

Pre-impact, *in-situ*, and post-impact results together affirm that differences in deformation behavior, failure modes, and relative energy absorption between the two PEs can be attributed to a competition between average rates of loading and chain relaxation. At $T_0 = -120$°C, both HDPE targets showed extensive cracking and fragmented completely. Conversely, the UHMWPE samples resisted widespread cracking but developed cone cracks around their perforations that generated large annular spall fragments. Debris clouds for both −120°C PE plates were populated with distinct target fragments. At room temperature, the UHMWPE targets fragmented extensively, whereas HDPE samples underwent significant thermal softening/melting and visco-plastic flow. UHMWPE

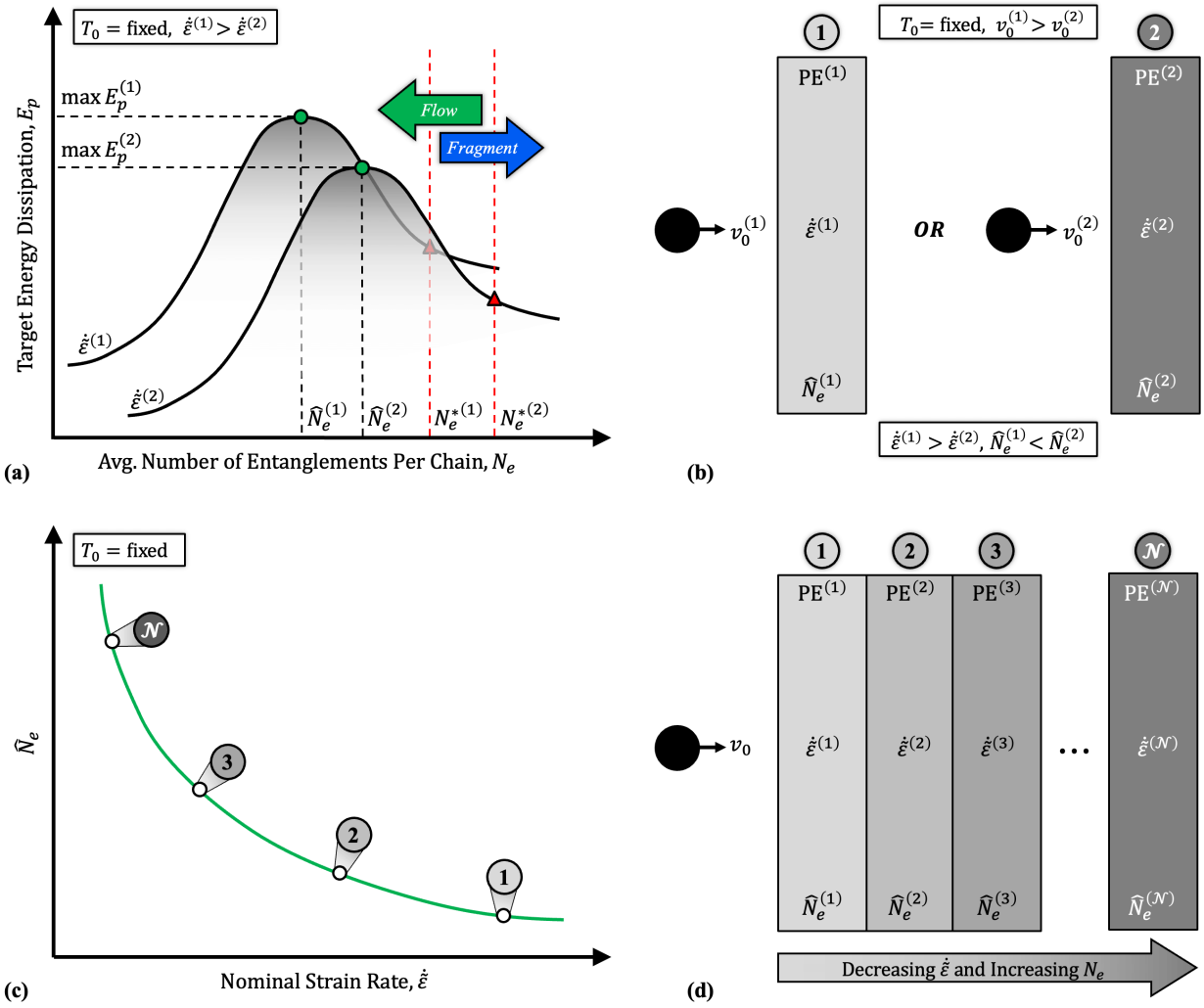

Figure 12: PE target energy absorption optimization: (a, b) the number of entanglements resulting in maximum E_p ($\hat{N}_e$) decreases with increasing v_0 and thus average strain rate ($\dot{\bar{\varepsilon}}$). $\hat{N}_e$ is less than $N_e^* = f(T_0, \dot{\bar{\varepsilon}}, \dots)$, the N_e value defining PE's transition from bulk quasi-brittle fragmentation to large-scale plastic deformation/flow at a given v_0, T_0, and projectile-target combination. (c) For fixed T_0, $\hat{N}_e$ decreases with increasing average strain rate. (d) A layered PE plate protective structure where, give a threat envelope (v_0, d_p, ...), each i-th layer ($i = 1, 2, 3, \dots, \mathcal{N}$) is tuned to dissipate the maximum energy for its local anticipated average strain rate. The plates are chosen to be more entangled as strain rate decreases.

debris clouds consisted of distinct fragments, while HDPE debris clouds were akin to expanding, web-like networks of interconnected molten fibrils, observations consistent with previous work. Heating the UHMWPE targets to 140°C increased the amount of flowing/molten material in the debris clouds. Yet, this enhanced flow ultimately gave way to widespread melt fracture, resulting in bulk UHMWPE fragmentation even when impacted above its T_m. The 140°C HDPE samples instead exhibited increased high-rate softening, melting, and flow without fracturing, leading to the

formation of membrane-like debris clouds that underwent extreme expansion without rupture. All targets exhibited charring and discoloration indicative of thermal degradation from impact-induced heating, in line with predictions. In general, lowering T_0 for fixed N_e inhibited high-rate chain motion analogously to increasing N_e at fixed T_0, making HDPE behave more like UHMWPE when subjected to similar HVIs. The opposite was also observed. Increasing v_0 heightened fracture/fragmentation susceptibility in both PEs by elevating strain rates beyond their rates of chain disentanglement and reorientation. The PE that lost less mass, had smaller perforations, and better absorbed energy generally exhibited the most visco-plastic flow without subsequent bulk fragmentation.

These observations suggest a critical N_e value exists, which, given constant v_0, T_0, and projectile-target combination, marks a PE target's HVI response shift from widespread fragmentation to bulk thermal softening/melting and flow. Consequently, for the same impact conditions, there is an optimal N_e value that maximizes PE target energy absorption. Raising v_0 or lowering T_0 necessitates a decrease in N_e to maintain the molecular mobility essential for optimal energy absorption. Hence, a layered, strain-rate-tuned PE protective structure is viable.

Funding: This research is based upon work supported by the National Science Foundation (NSF) Graduate Research Fellowship under Grant No. 1746932. The views and conclusions contained in this document are those of the authors and should not be interpreted as representing the official policies, either expressed or implied, of the U.S. Government. The U.S. Government is authorized to reproduce and distribute reprints for Government purposes notwithstanding any copyright notation herein.

Author contributions: T.E.L, E.L.T, J.A.R, and C.U.P. conceived the project. J.A.R., A.M., and S.D. executed the experiments. P.T.M performed finite element meshing and simulations. J.A.R, P.T.M., and J.W.W designed simulations and analyzed results. J.A.R. and T.E.L wrote the manuscript with input from all the authors.

Competing interests: The authors declare that they have no competing interests.

Data and materials availability: All data needed to evaluate the conclusions in the paper are present in the paper and/or the Supplementary Materials.

Supplementary materials:

Supplementary Text

Figures S1 to S8

Tables S1 to S2

References and Notes

1. E. L. Christiansen, *Meteoroid/debris shielding*, Tech. rep., National Aeronautics and Space Administration, Lyndon B. Johnson Space . . . (2003).

2. E. L. Christiansen, *et al.*, Handbook for designing MMOD protection. *NASA Johnson Space Center, NASA/TM-2009-214785* (2009).

3. H. M. Sayler, *Hypersonic weapons: Background and issues for Congress* (Congressional Research Service) (2019).

4. R. O'Rourke, Navy Lasers, Railgun, and Hypervelocity Projectile: Background and Issues for Congress. *Congressional Research Service* **17** (2017).

5. J. M. Acton, Hypersonic boost-glide weapons. *Science & Global Security* **23** (3), 191–219 (2015).

6. J. D. Walker, *Modern impact and penetration mechanics* (Cambridge university press) (2021).

7. J. D. Walker, From columbia to discovery: Understanding the impact threat to the space shuttle. *International journal of impact engineering* **36** (2), 303–317 (2009).

8. W. P. Schonberg, A. J. Bean, K. Darzi, *Hypervelocity impact physics*, Tech. rep., NASA (1991).

9. S. Signetti, A. Heine, Transition regime between high-velocity and hypervelocity impact in metals–a review of the relevant phenomena for material modeling in ballistic impact studies. *International Journal of Impact Engineering* **167**, 104213 (2022).

10. J. A. Rogers, *et al.*, The pursuit of hypervelocities: A review of two-stage light gas gun aeroballistic ranges. *International Journal of Impact Engineering* p. 104861 (2023).

11. R. Thirsk, A. Kuipers, C. Mukai, D. Williams, The space-flight environment: the International Space Station and beyond. *Cmaj* **180** (12), 1216–1220 (2009).

12. O. Uyanna, H. Najafi, Thermal protection systems for space vehicles: A review on technology development, current challenges and future prospects. *Acta Astronautica* **176**, 341–356 (2020).

13. E. Christiansen, J. Crews, J. Williamsen, J. Robinson, A. Nolen, Enhanced meteoroid and orbital debris shielding. *International Journal of Impact Engineering* **17** (1-3), 217–228 (1995).

14. J. Moonen, *et al.*, Evaluating UHMWPE-stuffed aluminium foam sandwich panels for protecting spacecraft against micrometeoroid and orbital debris impact. *International Journal of Impact Engineering* **180**, 104668 (2023).

15. M. Jacobs, J. Van Dingenen, Ballistic protection mechanisms in personal armour. *Journal of materials science* **36** (13), 3137–3142 (2001).

16. N. Kawai, M. Nagano, S. Hasegawa, E. Sato, In-situ observation of damage evolution in polycarbonate subjected to hypervelocity impact. *International Journal of Impact Engineering* **142**, 103584 (2020).

17. K. Qu, *et al.*, Ballistic performance of multi-layered aluminium and UHMWPE fibre laminate targets subjected to hypervelocity impact by tungsten alloy ball. *Composite Structures* **253**, 112785 (2020).

18. S. Khatiwada, C. A. Armada, E. V. Barrera, Hypervelocity impact experiments on epoxy/ultra-high molecular weight polyethylene fiber composites reinforced with single-walled carbon nanotubes. *Procedia Engineering* **58**, 4–10 (2013).

19. N. Kawai, *et al.*, Stress wave and damage propagation in transparent materials subjected to hypervelocity impact. *Procedia Engineering* **103**, 287–293 (2015).

20. K. Callahan, W. F. Heard, S. Kundu, High Strain Rate Failure Behavior of Polycarbonate Plates due to Hypervelocity Impact. *Macromolecules* **55** (21), 9640–9649 (2022).

21. A. Kozhushko, A. Sinani, Hypervelocity impact for brittle targets. *International journal of impact engineering* **29** (1-10), 391–396 (2003).

22. J. A. Rogers, *et al.*, Hypervelocity impact response of monolithic UHMWPE and HDPE plates. *International Journal of Impact Engineering* **161**, 104081 (2022).

23. J.-H. Cha, Y. Kim, S. K. S. Kumar, C. Choi, C.-G. Kim, Ultra-high-molecular-weight polyethylene as a hypervelocity impact shielding material for space structures. *Acta Astronautica* **168**, 182–190 (2020).

24. K. Ohtani, *et al.*, A study of hypervelocity impact on cryogenic materials. *International journal of impact engineering* **33** (1-12), 555–565 (2006).

25. D. Numata, *et al.*, HVI tests on CFRP laminates at low temperature. *International Journal of Impact Engineering* **35** (12), 1695–1701 (2008).

26. B. Wells, Hypervelocity impact tests on coated thermoplastic films at cryogenic and elevated temperatures. *International journal of impact engineering* **33** (1-12), 855–861 (2006).

27. W. Xie, *et al.*, High velocity impact tests on high temperature carbon-carbon composites. *Composites Part B: Engineering* **98**, 30–38 (2016).

28. C. R. Siviour, J. L. Jordan, High strain rate mechanics of polymers: a review. *Journal of Dynamic Behavior of Materials* **2**, 15–32 (2016), doi:10.1007/s40870-016-0052-8.

29. I. Mohagheghian, G. McShane, W. Stronge, Impact perforation of monolithic polyethylene plates: projectile nose shape dependence. *International Journal of impact engineering* **80**, 162–176 (2015).

30. J. M. Kelly, Ultra-high molecular weight polyethylene. *Journal of Macromolecular Science, Part C: Polymer Reviews* **42** (3), 355–371 (2002).

31. S. M. Aharoni, Correlations between chain parameters and failure characteristics of polymers below their glass transition temperature. *Macromolecules* **18** (12), 2624–2630 (1985).

32. A. M. Donald, E. J. Kramer, Effect of molecular entanglements on craze microstructure in glassy polymers. *Journal of Polymer Science: Polymer Physics Edition* **20** (5), 899–909 (1982).

33. P. G. Whitten, H. R. Brown, Polymer entanglement density and its influence on interfacial friction. *Physical Review E* **76** (2), 026101 (2007).

34. P. C. Painter, M. M. Coleman, *Essentials of polymer science and engineering* (DEStech Publications, Inc., Lancaster, Pennsylvania) (2009).

35. M. M. Xu, G. Y. Huang, S. S. Feng, G. J. McShane, W. J. Stronge, Static and dynamic properties of semi-crystalline polyethylene. *Polymers* **8** (2016), doi:10.3390/polym8040077.

36. J.-F. Agassant, P. Avenas, P. J. Carreau, B. Vergnes, M. Vincent, *Polymer processing: principles and modeling* (Carl Hanser Verlag GmbH Co KG) (2017).

37. R. K. Krishnaswamy, Q. Yang, L. Fernandez-Ballester, J. A. Kornfield, Effect of the distribution of short-chain branches on crystallization kinetics and mechanical properties of high-density polyethylene. *Macromolecules* **41** (5), 1693–1704 (2008).

38. B. Bersted, On the effects of very low levels of long chain branching on rheological behavior in polyethylene. *Journal of applied polymer science* **30** (9), 3751–3765 (1985).

39. S. Austin, *et al.*, The high-velocity impact of Dyneema® and Spectra® laminates: implementation of a simple thermal softening model. *Procedia Engineering* **204**, 51–58 (2017).

40. E. Brown, *et al.*, Influence of molecular conformation on the constitutive response of polyethylene: a comparison of HDPE, UHMWPE, and PEX. *Experimental Mechanics* **47** (3), 381–393 (2007).

41. A. I. Mourad, H. Elsayed, D. Barton, M. Kenawy, L. Abdel-Latif, Ultra high molecular weight polyethylene deformation and fracture behaviour as a function of high strain rate and triaxial state of stress. *International Journal of Fracture* **120** (3), 501–515 (2003).

42. E. Brown, C. Trujillo, G. Gray III, Influence of polyethylene molecular conformation on Taylor impact measurements: a comparison of HDPE, UHMWPE, and PEX, in *AIP Conference Proceedings* (American Institute of Physics), vol. 955 (2007), pp. 691–694.

43. J. Furmanski, C. M. Cady, E. N. Brown, Time–temperature equivalence and adiabatic heating at large strains in high density polyethylene and ultrahigh molecular weight polyethylene. *Polymer* **54** (1), 381–390 (2013), doi:https://doi.org/10.1016/j.polymer.2012.11.010.

44. R. W. Nunes, J. R. Martin, J. F. Johnson, Influence of molecular weight and molecular weight distribution on mechanical properties of polymers. *Polymer Engineering & Science* **22** (4), 205–228 (1982).

45. J. Karger-Kocsis, E. Moos, I. Mudra, J. Varga, Effects of molecular weight on the perforation impact behavior of injection-molded plaques of α-and β-phase isotactic polypropylenes. *Journal of Macromolecular Science—Physics* **38** (5-6), 647–662 (1999).

46. A. Van der Wal, J. Mulder, R. Gaymans, Fracture of polypropylene: The effect of crystallinity. *Polymer* **39** (22), 5477–5481 (1998).

47. B. Li, G. Gong, B.-H. Xie, W. Yang, M.-B. Yang, Influence of molecular weight on impact fracture behavior of injection molded high density polyethylene: scanning electron micrograph observations. *Journal of applied polymer science* **109** (2), 1161–1167 (2008).

48. I. Brough, R. Haward, G. Healey, A. Wood, Scanning electron micrographs of high density polyethylene fracture surfaces. *Polymer* **45** (10), 3115–3123 (2004).

49. N. Brooks, M. Ghazali, R. Duckett, A. Unwin, I. Ward, Effects of morphology on the yield stress of polyethylene. *Polymer* **40** (4), 821–825 (1999), doi:https://doi.org/10.1016/S0032-3861(98)00324-3.

50. B. A. Schrauwen, R. P. Janssen, L. E. Govaert, H. E. Meijer, Intrinsic deformation behavior of semicrystalline polymers. *Macromolecules* **37** (16), 6069–6078 (2004).

51. C. Price, *Influence of thermal and dynamic viscoelastic properties of polymers on low-mass, high-velocity penetrations*, Master's thesis, Mississippi State University (2016).

52. I.-C. Yeh, J. W. Andzelm, G. C. Rutledge, Mechanical and structural characterization of semicrystalline polyethylene under tensile deformation by molecular dynamics simulations. *Macromolecules* **48** (12), 4228–4239 (2015).

53. S. Lee, G. C. Rutledge, Plastic deformation of semicrystalline polyethylene by molecular simulation. *Macromolecules* **44** (8), 3096–3108 (2011).

54. D. Hossain, *et al.*, Molecular dynamics simulations of deformation mechanisms of amorphous polyethylene. *Polymer* **51** (25), 6071–6083 (2010).

55. M. Bowering, *Strain rate effects on energy dissipation during hypervelocity penetration of polymeric materials*, Master's thesis, Mississippi State University (2018).

56. Y. Sui, *et al.*, Eminent differences in cryogenic toughness of ultra-high molecular weight polyethylene with different entanglement densities. *Journal of Applied Polymer Science* **140** (7), e53475 (2023).

57. M. Amjadi, A. Fatemi, Tensile behavior of high-density polyethylene including the effects of processing technique, thickness, temperature, and strain rate. *Polymers* **12** (9), 1857 (2020).

58. I. I. Salakhov, *et al.*, Low-temperature mechanical properties of high-density and low-density polyethylene and their blends. *Polymers* **13** (11), 1821 (2021).

59. L. Fetters, D. Lohse, D. Richter, T. Witten, A. Zirkel, Connection between polymer molecular weight, density, chain dimensions, and melt viscoelastic properties. *Macromolecules* **27** (17), 4639–4647 (1994).

60. Mitsubishi Chemical Advanced Materials, Reading, PA, *TIVAR® 1000 virgin UHMW-PE: product datasheet*, https://www.mcam.com/na-en/products/engineering-plastics/standard/tivarr-uhmw-pe-family-of-products/tivarr-1000/.

61. King Plastic Corporation, North Port, FL, *King Performance Commodities HDPE: material and physical datasheet* (2014), https://www.kingplastic.com/wp-content/uploads/2014/05/King-KPC-HDPE-Physical-Properties.pdf.

62. D. Jauffres, O. Lame, G. Vigier, F. Dore, Microstructural origin of physical and mechanical properties of ultra high molecular weight polyethylene processed by high velocity compaction. *Polymer* **48** (21), 6374–6383 (2007).

63. J. Min, B. Lee, J.-S. Lee, Development of synthetic resin-based mortar for low-activation and neutron shields. *Construction and Building Materials* **124**, 992–998 (2016).

64. C. Zhang, *et al.*, High elastic modulus polyethylene–A two-stage multi-axial rolling and orientation process. *Polymer* **256**, 125180 (2022).

65. K. Patel, S. H. Chikkali, S. Sivaram, Ultrahigh molecular weight polyethylene: Catalysis, structure, properties, processing and applications. *Progress in polymer science* **109**, 101290 (2020).

66. V. Litvinov, M. Ries, T. Baughman, A. Henke, P. Matloka, Chain entanglements in polyethylene melts. Why is it studied again? *Macromolecules* **46** (2), 541–547 (2013).

67. L. J. Fetters, D. J. Lohse, S. T. Milner, W. W. Graessley, Packing length influence in linear polymer melts on the entanglement, critical, and reptation molecular weights. *Macromolecules* **32** (20), 6847–6851 (1999).

68. J. A. Rogers, *et al.*, The Texas A&M University Hypervelocity Impact Laboratory: A modern aeroballistic range facility. *Review of Scientific Instruments* **93** (8) (2022).

69. J. Warren, *et al.*, Hypervelocity impacts on honeycomb core sandwich panels filled with shear thickening fluid. *International journal of impact engineering* **150**, 103803 (2021).

70. G. R. Johnson, Analysis of Elastic-Plastic Impact Involving Severe Distortions. *Journal of Applied Mechanics* **43** (3), 439–444 (1976), doi:10.1115/1.3423887.

71. G. R. Johnson, R. A. Stryk, S. R. Beissel, T. J. Holmquist, An algorithm to automatically convert distorted finite elements into meshless particles during dynamic deformation. *International Journal of Impact Engineering* **27** (10), 997–1013 (2002).

72. E. Grüneisen, Theorie des festen Zustandes einatomiger Elemente. *Annalen der Physik* **344** (12), 257–306 (1912).

73. G. R. Johnson, A constitutive model and data for materials subjected to large strains, high strain rates, and high temperatures. *Proc. 7th Inf. Sympo. Ballistics* pp. 541–547 (1983).

74. G. R. Johnson, W. H. Cook, Fracture characteristics of three metals subjected to various strains, strain rates, temperatures and pressures. *Engineering fracture mechanics* **21** (1), 31–48 (1985).

75. J. Rogers, P. T. Mead, J. Wilkerson, T. E. Lacy, N. Williams, Simulating Hypervelocity Impacts to High-Density Polyethylene, in *AIAA SCITECH 2023 Forum* (2023), p. 2021.

76. R. C. Huber, *et al.*, In situ x-ray diffraction of high density polyethylene during dynamic drive: Polymer chain compression and decomposition. *Journal of Applied Physics* **130** (17) (2021).

77. M. E. Backman, W. Goldsmith, The mechanics of penetration of projectiles into targets. *International Journal of Engineering Science* **16** (1), 1–99 (1978).

78. H. Yang, *et al.*, Thermal, rheological, and mechanical characterization of compression and injection molded ultra-high molecular weight polyethylene, high density polyethylene, and their blends. *Journal of Applied Polymer Science* **140** (7), e53484 (2023).

79. C. Xie, Interactive Heat Transfer Simulations for Everyone. *The Physics Teacher* **50** (4), 237–240 (2012).

80. S. Signetti, A. Heine, Characterization of the transition regime between high-velocity and hypervelocity impact: Thermal effects and energy partitioning in metals. *International Journal of Impact Engineering* **151**, 103774 (2021).

81. R. F. Prater, *et al.*, *Hypervelocity impact: material strength effects on crater formation and shock propagation in three aluminum alloys*, Ph.D. thesis, Air Force Institute of Technology. (1970).

82. F. Dowell, *Simple EOS for linear (high-density) polyethylene (Marlex)*, Tech. rep., Los Alamos National Lab.(LANL), Los Alamos, NM (United States) (1982).

Supplementary Materials for Temperature Dependence of the Hypervelocity Impact Response of Polyethylene Plates from T_g to T_m

Jacob A. Rogers[1,2,3*], Aniket Mote[1], Sidney Davis[1], Paul T. Mead[4], Charles U. Pittman, Jr.[5], Edwin L. Thomas[2], Justin W. Wilkerson[1,2], Thomas E. Lacy, Jr.[1**]

[1]Department of Mechanical Engineering, Texas A&M University, College Station, TX 77843.

[2]Department of Material Science and Engineering, Texas A&M University, College Station, TX 77843.

[3] High Explosives Science and Technology, Q-5, Los Alamos National Laboratory, Los Alamos, NM 87545.

[4]U.S. Army Engineer Research and Development Center, Vicksburg, MS 39180.

[5]Department of Chemistry, Mississippi State University, Starkville, MS 39762.

[*]Corresponding author. Email: jacob_rogers@lanl.gov

[**]Corresponding author. Email: telacyjr@tamu.edu

This PDF file includes:

Supplementary Text

Figures S1 to S8

Tables S1 to S2

S1 Simple Two-Dimensional Heat Transfer Simulations for the PE Plates

2D heat transfer simulations in the fast-running Energy2D multi-physics software (version 3.0.3) (*79*) were used to estimate how the difference in the PE target's mid-plane (T_2) and surface (T_1) temperatures temporally evolved as it warmed and cooled. Energy2D combines fast finite-difference algorithms and a computational fluid dynamics (CFD) engine to solve the heat equation and the Navier-Stokes equation. Given that the PEs had similar thermal properties, only two simulations were run: one for $T_0 = -180$°C (warming) and one for $T_0 = 170$°C (cooling). Each simulated plate's cross-sectional dimensions (102 mm x 12.7 mm) matched those from the HVI experiments. The representative plate's thermal conductivity, specific heat capacity, and density were assigned values of 0.5 W/(K·m), 2.0 kJ/(kg·K), and 0.93 g/cm^3, respectively (*cf.* Table 1 in main document). The warming/cooling process was simulated for twenty minutes, with a time step of 0.01 seconds. The plates were isolated in a 250 mm x 250 mm "volume" of lab air at $T_\infty = 23$°C, which was descritized into a 100 x 100 square computation grid. For each plate, the difference between T_2 and T_1 varied over time but averaged around 6°C, with a standard deviation of about 0.7°C (Fig. S1a). Figures S1b and S1c present snapshots of the temperature fields around the targets, each taken about one minute into the simulation. The denser cold air flows downward, while the hotter air flows upward, due to gravity.

S2 Target Boundary Considerations

In-plane reflected waves from the target's boundary, influenced by the materials, shapes, and relative impact velocity of the projectile and target, can affect the dynamics of penetration and/or perforation. If the time taken for perforation (t_p) is significantly shorter than the duration for the leading shock wave to travel from the impact point to the boundary and back (t_b), disruption of the perforation event from reflected waves is unlikely. Hence, evaluating the ratio t_p/t_b offers insight into potential boundary effects.

The time for a shock wave to travel to the boundary and back in a given axisymmetric target can be estimated as

$$t_b \approx 2\frac{r_b}{U_t}, \tag{S1}$$

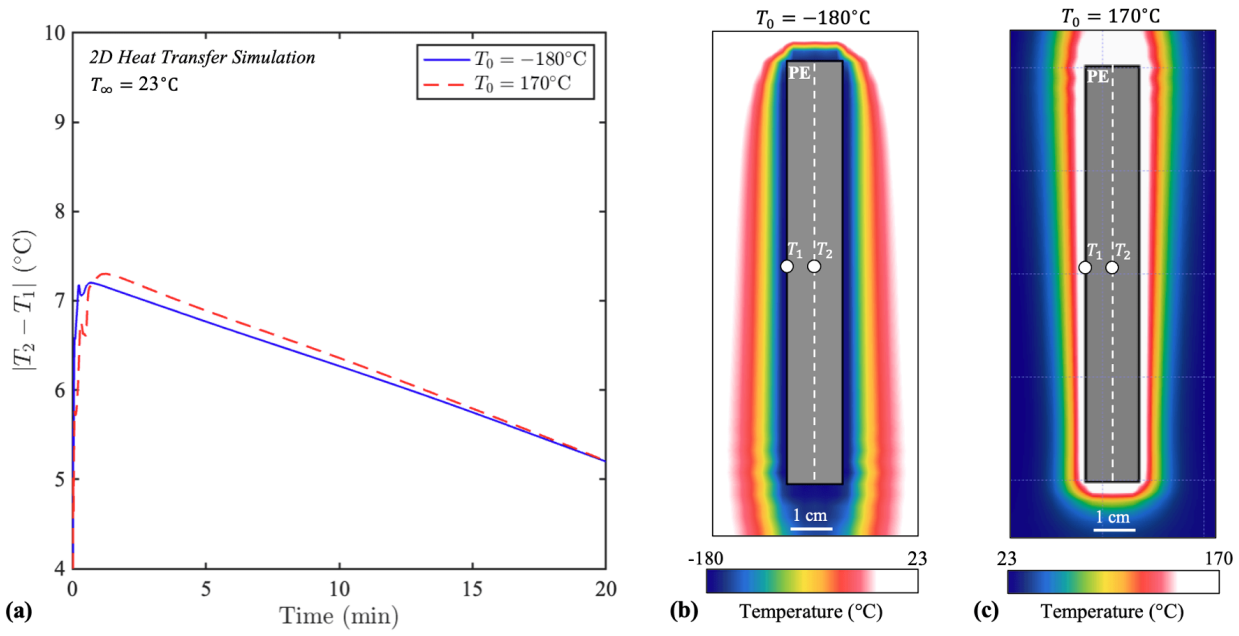

Figure S1: 2D heat transfer simulation results for a representative PE plate: (a) Displays the temperature differences between the target mid-plane (T_2) and surface (T_1) over time for $T_0 = -180°C$ and $T_0 = 170°C$. For both T_0, $|T_2 - T_1|$ averaged approximately 6°C with a standard deviation of 0.7°C. (b) and (c) Present snapshots of the temperature field surrounding the targets, both at approximately one minute into the simulation.

where r_b is the in-plane radius from the impact point to the target boundary and U_t is the shock velocity (a function of v_0). For simplicity, this analysis of boundary effects only considers HDPE as the target material, but the results would be similar for UHMWPE. U_t values for HDPE were sourced and extrapolated from Ref. (*76*). Similarly, noting that $v_{dc}/v_0 \lessapprox 0.5$ for the experiments in this study, the perforation/puncture time can be approximated as

$$t_p \approx \frac{2h_t}{v_0 + v_r} \approx \frac{2h_t}{v_0 + v_{dc}} \approx \frac{4}{3}\frac{h_t}{v_0}, \tag{S2}$$

where h_t is the target thickness, v_0 is the projectile impact velocity, and $v_r \sim v_{dc}$ is the projectile residual velocity after impact. For all experiments, $r_b = 3.8$ cm. Using v_0 values that span the tested range ($v_0 = 2.0$–6.5 km/s), values for t_b, t_p, and t_p/t_b were approximated (Table S1). These simple calculations show that for all impacts, the perforation time was much less than the wave travel time ($t_p \lesssim 0.5t_b$), indicating reflected in-plane waves did not influence experimental perforation dynamics (Fig. S2).

Table S1: Approximations of wave travel time (t_b), perforation time (t_p), and their ratio (t_p/t_b) for the PE sample geometry and fixturing. Calculated values are based on the target's approximate shock velocity (U_t), projectile impact and residual velocities (v_0 and $v_r \sim v_{dc}$), and in-plane radius from the impact point to the boundary (r_b). The analysis shows that for all impacts, the perforation time is significantly shorter than the wave travel time.

No.	v_0 (km/s)	v_{dc} (km/s)	h_t (mm)	t_p (µs)	r_b (cm)	t_b (µs)	t_p/t_b (%)
1	2.00	1.00	12.7	8.47	3.81	13.1	64
2	2.50	1.25	12.7	6.77	3.81	12.7	53
3	3.00	1.50	12.7	5.64	3.81	11.6	49
4	3.50	1.75	12.7	4.84	3.81	10.7	45
5	4.00	2.00	12.7	4.23	3.81	9.9	43
6	4.50	2.25	12.7	3.76	3.81	9.2	41
7	5.00	2.50	12.7	3.39	3.81	8.6	39
8	5.50	2.75	12.7	3.08	3.81	8.1	38
9	6.00	3.00	12.7	2.82	3.81	7.6	37
10	6.50	3.25	12.7	2.61	3.81	7.2	36

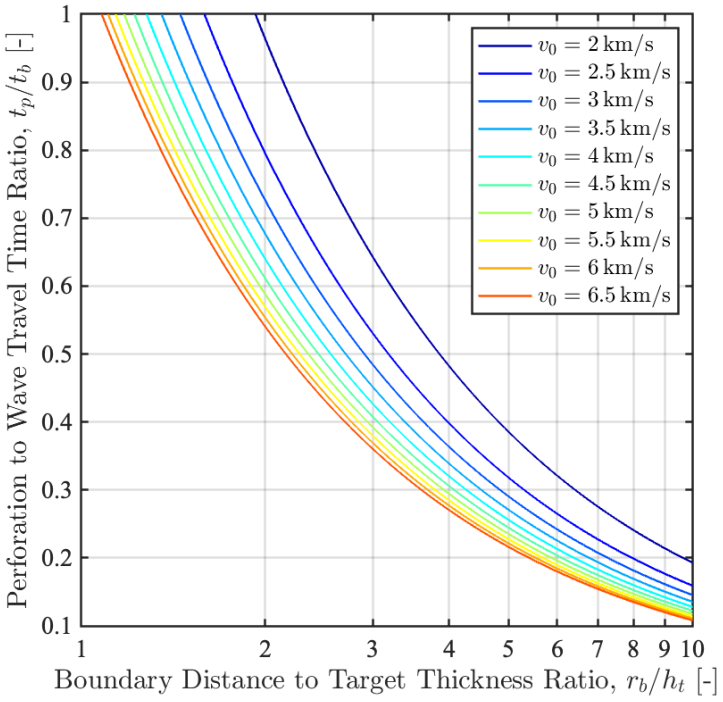

Figure S2: The effect of target-center-to-boundary distance (r_b) and target thickness (h_t) on the projectile perforation time (t_p) compared to the longitudinal stress wave travel time (t_b) across various impact velocities (v_0). The projectile size is assumed significantly smaller than the distance from target center to boundary ($d_p \ll r_b$).

S3 High-Speed Images of HVIs Showing Debris Cloud Development

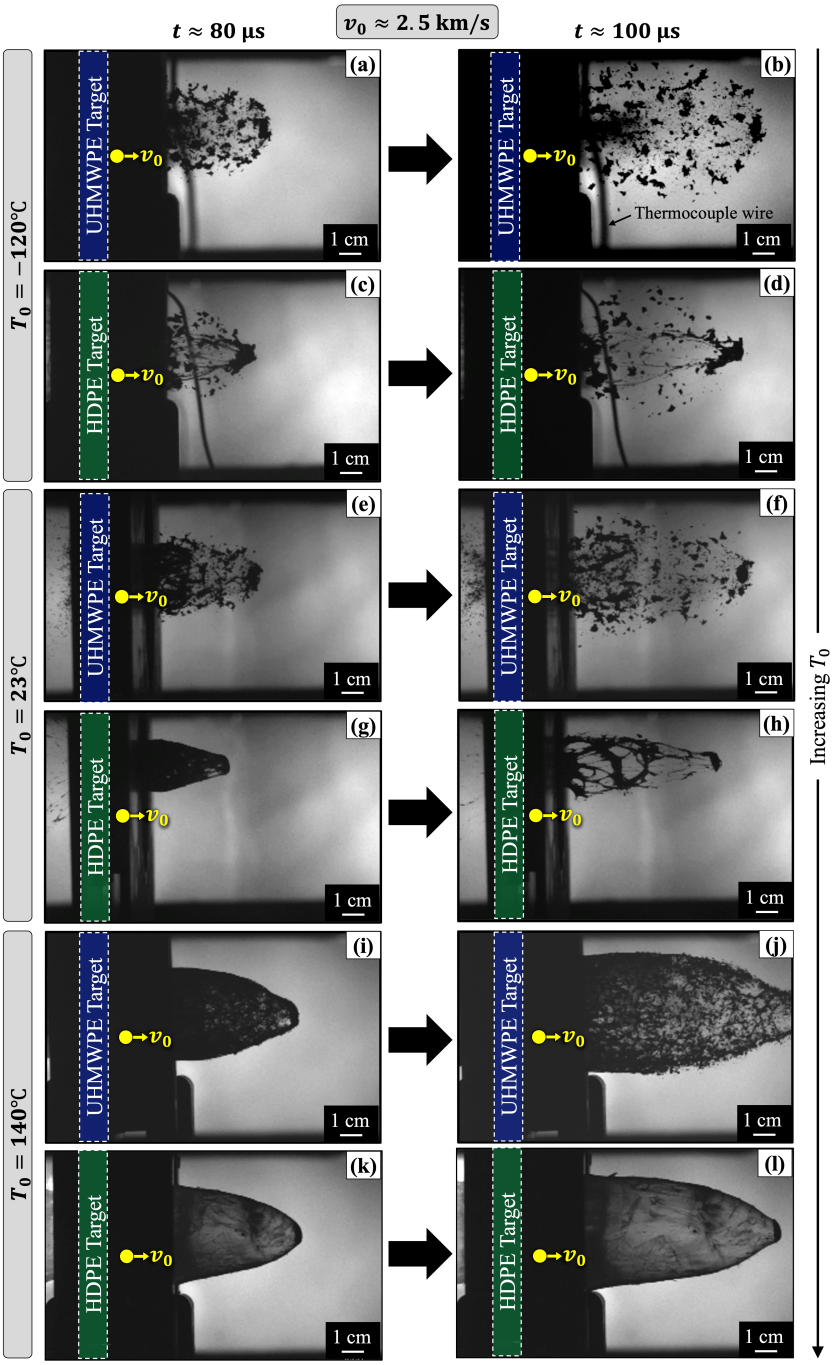

Figure S3: Debris clouds from HVIs of $d_p = 6.35$ mm aluminum spheres into 12.7 mm thick UHMWPE and HDPE plates at $v_0 \approx 2.5$ km/s, captured at two time instances ($t \approx 80$ µs and 100 µs; columns, in ascending order) and at three target temperatures (rows, in ascending order): (a–d) $T_0 = -120$°C, (e–h) $T_0 = 23$°C, and (i–l) $T_0 = 140$°C.

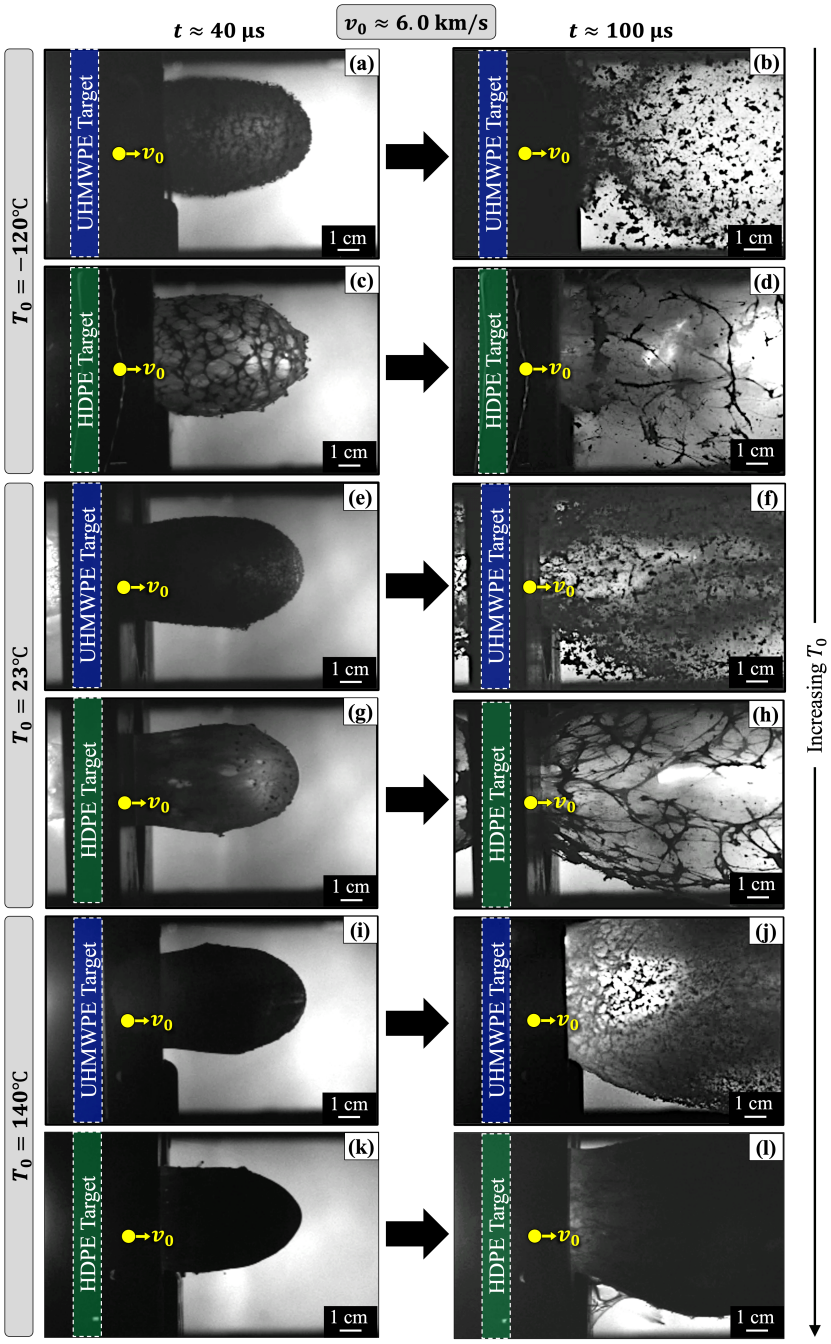

Figure S4: Debris clouds from HVIs of d_p = 6.35 mm aluminum spheres into 12.7 mm thick UHMWPE and HDPE plates at $v_0 \approx 6.0$ km/s, captured at two time instances ($t \approx 40$ µs and 100 µs; columns, in ascending order) and at three target temperatures (rows, in ascending order): (a–d) $T_0 = -120$°C, (e–h) $T_0 = 23$°C, and (i–l) $T_0 = 140$°C.

S4 Results of HVI Numerical Simulations

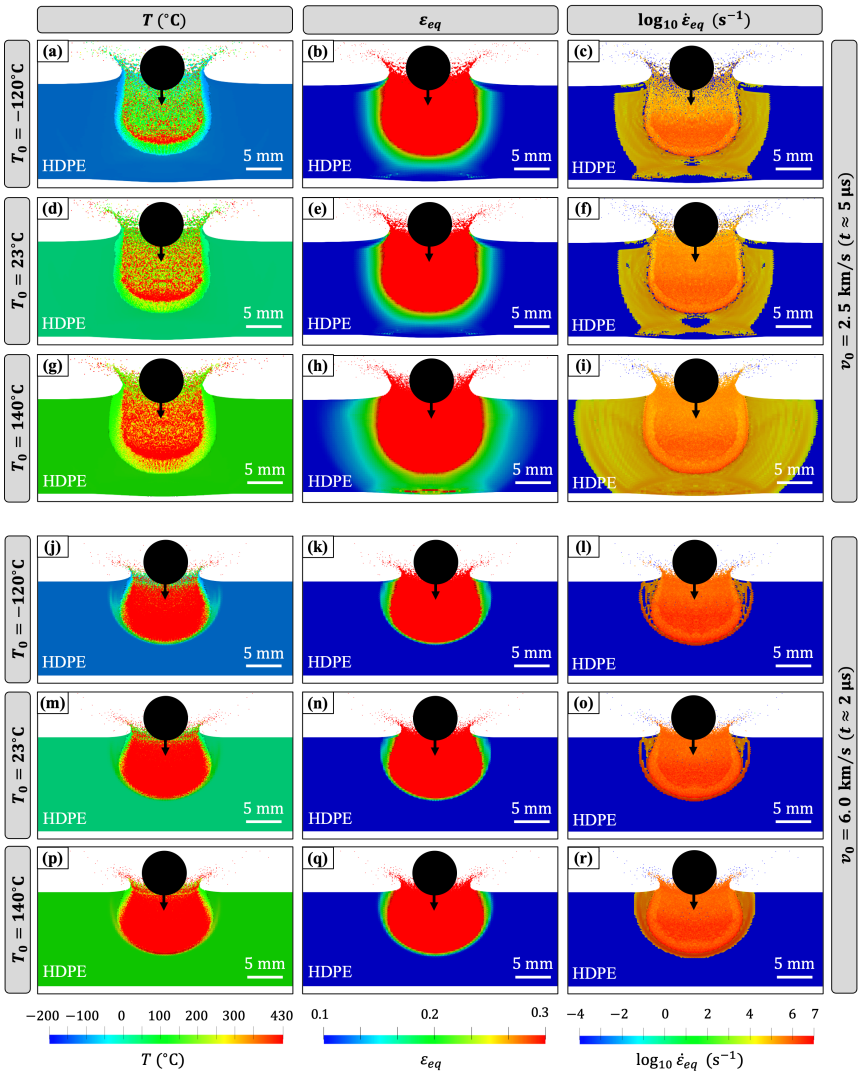

Figure S5: Simulation snapshots of temperature T, equivalent plastic strain ε_{eq}, and equivalent plastic strain rate ($\dot{\varepsilon}_{eq}$) for d_p = 6.35 mm aluminum sphere HVIs into 12.7 mm thick representative HDPE plates at (a–i) $v_0 \approx$ 2.5 km/s and (j–r) $v_0 \approx$ 6.0 km/s. Snapshots are shown at times corresponding to when the target is halfway perforated. Simulated projectiles were hidden from the snapshots to better showcase the targets' conditions. A scaled projectile *icon* is superimposed on each image for reference. For each v_0, the snapshot time reflects the moment the target is approximately halfway perforated. Target temperatures reach the thermal degradation temperature of HDPE (T = 430°C), and strain rates reach $\dot{\varepsilon}_{eq} = 10^7$ s^{-1}. Material models and parameters were sourced from Ref. (*75*).

S5 Additional Target Images

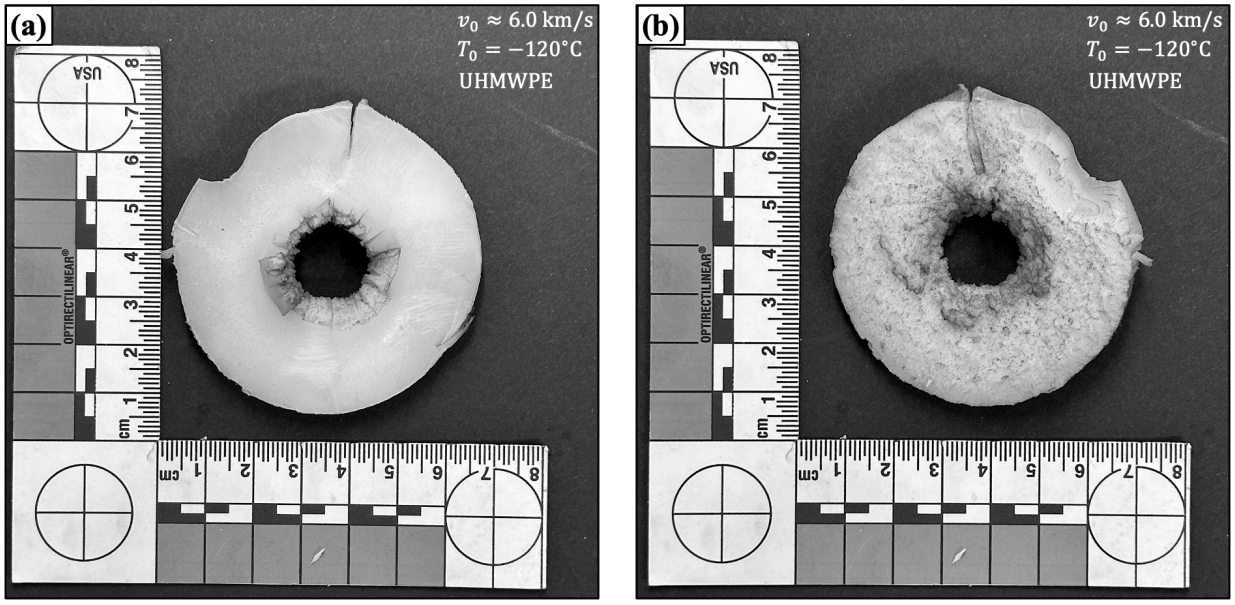

Figure S6: Front (left) and back side (right) images of the target spall fragment due to cone fracture of the -120°C UHMWPE target impacted at 6.0 km/s (*cf.* Fig. 8d).

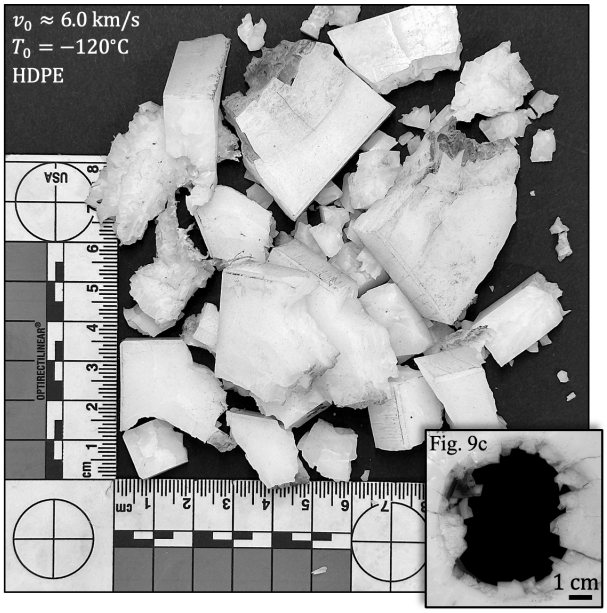

Figure S7: Fragments of the −120°C HDPE plate impacted at $v_0 \approx 6.0$ km/s. An image displaying the perforation was captured before the target was removed from the fixture (see inset and Fig. 9d).

S6 The Transition Velocity Regime for UHMWPE and HDPE

For a specific projectile-target material pair, discerning the transition from high-velocity impact conditions (where material response is dominated by strength) to hypervelocity impact phenomena (characterized by hydrodynamic behavior) is crucial for understanding the materials' states, as well as their primary deformation and failure mechanisms. A straightforward method for defining this transition regime entails identifying the impact velocities that result in material shocks strong enough to trigger incipient and complete melting of the projectile/target (*80*).[4] These critical velocities can be approximated using the one-dimensional (1D) Rankine-Hugoniot equations, which, for a coordinate system moving with the shock front traveling through a medium, can be expressed as

$$\frac{u}{U} = \left(1 - \frac{\rho_0}{\rho}\right) \qquad \textit{mass conservation}, \tag{S3}$$

$$p - p_0 = \rho_0 U u \qquad \textit{momentum conservation}, \tag{S4}$$

$$e - e_0 = \frac{1}{2}(p + p_0)\left(1 - \frac{\rho_0}{\rho}\right) = \frac{1}{2}\rho_0 u^2 \qquad \textit{energy conservation}, \tag{S5}$$

where u represents the material particle velocity; U the shock front velocity; ρ_0 and ρ the densities before and after the shock, respectively; p_0 and p the momenta before and after the shock, respectively; and e_0 and e the internal energies before and after the shock, respectively. Equations (S4)–(S5), combined with the kinematic condition $v_0 = u_p + u_t$, can be used to partition the specific internal energy of the projectile and target upon impact:

$$e_p = \left(\frac{u_p/u_t}{1 + u_p/u_t}\right)^2 k_0, \tag{S6}$$

and

$$e_t = \frac{u_p/u_t}{(1 + u_p/u_t)^2} k_0, \tag{S7}$$

where subscripts p and t denote the projectile and target materials, respectfully, and $k_0 = \frac{1}{2}\rho_{0,p} v_0^2$. An equation of state (EOS) is also required. For simplicity, a simple EOS was used in this work,

[4]The following transition regime derivation/definition was first reported by Signetti *et al.* (*80*).

i.e.,

$$U_{(p/t)} = s_{(p/t)} u_{(p/t)} + a_{(p/t)} \tag{S8}$$

where s is an empirical fitting parameter and $a = \sqrt{K/\rho_0}$ is the material sound velocity at zero pressure (K is the material bulk modulus). Equations (S6)–(S8) can be used to calculate the "trapped" residual internal energy in the projectile/target that can contribute to heating:

$$e_{h,(p/t)} = e_{(p/t)} - \frac{1}{\rho_{(p/t)}} \int_{\rho_{0,(p/t)}}^{\rho_{(p/t)}} r \, d\rho \Big|_{S=\text{const.}}, \tag{S9}$$

where the second term represents the reversible energy from isentropic (S = const) expansion due to pressure release (*i.e.*, rarefaction wave). Incipient melting for each material occurs when the internal energy within it equals

$$e_{m,(p/t)} = \rho_{0,(p/t)} \int_{T_0}^{T_{m,(p/t)}} c_{v,(p/t)}(T) \, dT, \tag{S10}$$

where T_m is the melting temperature of the material, $c_v(T)$ is its specific heat capacity at constant volume, and T is the variable temperature. Complete melting of the material occurs when

$$e_{h,(p/t)}(v_0) = e_{m,(p/t)} + e_{fus,(p/t)}, \tag{S11}$$

where $e_{fus,(p/t)}$ is the enthalpy of fusion. Thus, for a given projectile-target material combination, the transition velocity regime can be defined as

$$\min(v_{m,p}, v_{m,t}) < v_0 < \max(v_{fus,p}, v_{fus,t}), \tag{S12}$$

where $v_{m,(p/t)}$ and $v_{fus,(p/t)}$ are the impact velocities leading to incipient and complete melting, respectively, of the projectile/target material.

This method was applied here to estimate the transition regime for the aluminum projectiles impacting the PE targets. Given their similar thermal properties and densities, both PEs were characterized succinctly in one calculation using representative values for T_m, ρ_0, c_v, e_{fus}, a, and s. The parameter values used for the projectile/target are summarized in Table S2. Figure S8 displays the residual specific internal energy in the projectile/target as a function of impact velocity. The

target undergoes a transition to predominantly hydrodynamic behavior at a relatively low velocity ($v_0 \sim 2.5$ km/s) compared to the aluminum sphere ($v_0 \sim 9.0$ km/s). Hence, the complete transition velocity regime is $2.0 < v_0 < 9.1$ km/s.

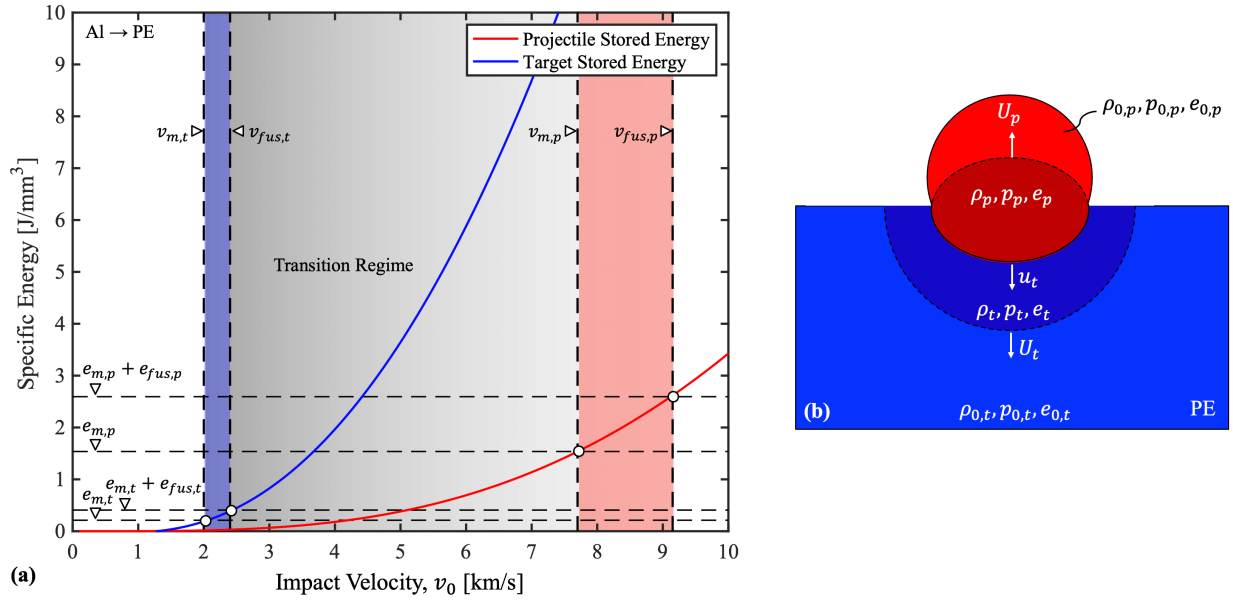

Figure S8: Transition velocity regime (high-velocity to hypervelocity) for an aluminum sphere impacting a HDPE plate, marked by the onset and complete melting of materials (*9*). This regime is defined for the sphere with initial density $\rho_{p,0}$, momentum $p_{p,0}$, and internal energy $e_{p,0}$, and for the HDPE plate with initial density $\rho_{t,0}$, momentum $p_{t,0}$, and internal energy $e_{t,0}$. The transition velocity region ranges from $v_{m,t} = 2.0$ km/s to $v_{fus,p} = 9.1$ km/s for both the projectile and target, and $v_{m,t} = 2.0$ km/s to $v_{fus,t} = 2.3$ km/s for the target alone. These calculations indicate PE targets melt and exhibit hydrodynamic behavior at velocities $v_0 \geq 2.5$ km/s.

Table S2: Material data for transition velocity regime calculations sourced from Refs. (*81, 82*).

No.	Parameter	Projectile (Al)	Target (PE)	Units
1	T_m	650	130	°C
2	ρ_0	2.70	0.95	g/cm^3
3	c_v	0.90	2.00	J/(g·°C)
4	e_{fus}	1.06	0.20	J/mm^3
5	a	5.25	2.88	km/s
6	s	1.37	1.68	···